

Signatures of UV radiation around low-mass protostars in Serpens with IRAM 30 m

Agnieszka Mirocha^{1,2}, Agata Karska^{2*}, Marcin Gronowski^{3,4}, Lars E. Kristensen⁵, Miguel Figueira⁶, Marcin Gładkowski^{2,7}, Łukasz Tychoniec⁸, Michał Żółtowski⁹

¹ Astronomical Observatory of the Jagiellonian University, ul. Orla 171, 30-244 Kraków, Poland

² Institute of Astronomy, Faculty of Physics, Astronomy and Informatics, Nicolaus Copernicus University, ul. Grudziądzka 5, 87-100 Toruń, Poland

³ Institute of Physical Chemistry Polish Academy of Sciences, ul. Kasprzaka 44/52, 01-224 Warszawa, Poland

⁴ Faculty of Physics, University of Warsaw, Pasteura 5, 02-093 Warsaw, Poland

⁵ Centre for Star and Planet Formation, Niels Bohr Institute and Natural History Museum of Denmark, University of Copenhagen, Øster Voldgade 5-7, DK-1350 Copenhagen K, Denmark

⁶ National Centre for Nuclear Research, ul. Pasteura 7, 02-093 Warszawa, Poland

⁷ Nicolaus Copernicus Astronomical Center, ul. Rabciańska 8, 87-100 Toruń, Poland

⁸ Leiden Observatory, Leiden University, P.O. Box 9513, NL-2300RA Leiden, The Netherlands

⁹ University of Le Havre, Laboratoire Ondes et Milieux Complexes, UMR CNRS 6294, 75 Rue Bellot, 76600 Le Havre, France

Received [Month] [Day], 2020; accepted [Month] [Day], 2020

ABSTRACT

Context. Ultraviolet radiation (UV) influences the physics and chemistry of star-forming regions, but its properties and significance toward low-mass protostars are still poorly-understood.

Aims. We aim to identify and characterise the UV radiation in the surroundings of low-mass protostars on $\sim 0.6 \times 0.6$ pc scales using the CN to HCN ratio previously used for high-mass protostars. We focus on comparisons between protostar and outflow positions in the Serpens star-forming region and the validation of the proposed UV tracer for the environment of low-mass protostars.

Methods. We present the $5' \times 5'$ maps of the Serpens Main encompassing 10 protostars observed with the EMIR receiver at IRAM 30 m in CN 1-0, HCN 1-0, CS 3-2, and their isotopologues. The radiative-transfer code RADEX and the chemical model Nahoon are used to determine column densities of molecules, gas temperature and density, and the UV field strength, G_0 .

Results. Spatial distribution of HCN and CS are well-correlated with the CO 6-5 from APEX tracing outflows. CN emission is spatially associated with the positions of protostars, and extends also to their immediate surroundings. Detection of the line wings in CN profiles suggests that at least some emission is produced in the outflows, likely as a product of HCN photodissociation. The ratio of CN to HCN total column densities ranges from 1 to 10 corresponding to $G_0 \approx 10^1 - 10^3$ for gas densities and temperatures typical for outflows of low-mass protostars.

Conclusions. UV radiation is identified towards both protostar and outflow positions. Its strength is corresponding with a **higher** end of the range determined from *Herschel* observations. From the chemical viewpoint, the CN and HCN ratio is a better tracer for UV fields characteristic for more massive protostars than for the low-mass star forming regions.

Key words. astrochemistry – stars: formation – ISM: molecules – ISM: individual objects: Serpens Main – Submillimeter: ISM

1. Introduction

Formation of low-mass stars is associated with many physical phenomena. The inside-out collapse of dense envelopes is accompanied by the ejection by bipolar outflows and the formation of embedded disks (Frank et al. 2014; Harsono et al. 2015). Ultraviolet (UV) radiation can be produced in mass accretion on the central object or bow shocks and irradiates the outflow cavities in the envelopes (Spaans et al. 1995; van Kempen et al. 2009a). The physical conditions and chemical composition in star-forming regions strictly depend on the characteristics of the above processes.

The importance of UV radiation for star formation was initially only considered in the context of the formation of massive stars, where central stars are the main source of UV photons

from early stages (Cesaroni 2005; Zinnecker & Yorke 2007). Detail chemical models of the envelopes and outflows with radiative transfer in 1 and 2D have been developed for high-mass protostars (Doty & Neufeld 1997; Stäuber et al. 2005; Bruderer et al. 2009). The far-UV radiation dissociates and ionizes molecules and atoms with ionization potentials below 13.6 eV; more energetic photons are easily absorbed in the surrounding interstellar medium (Gerin et al. 2016). Among the most useful diagnostics of the UV field in dense envelopes are abundances of hydrides and the column density ratio of CN and HCN (Stäuber et al. 2007). The corresponding UV field strengths are enhanced by at least 1-2 orders of magnitude compared to the interstellar radiation field and impact gas at temperatures of few hundred K (Stäuber et al. 2007; Benz et al. 2016). Yet, the CN and HCN ratio have not been used to probe the UV radiation in the envelopes of low-mass protostars so far.

* Corresponding author: Agata Karska
e-mail: agata.karska@umk.pl

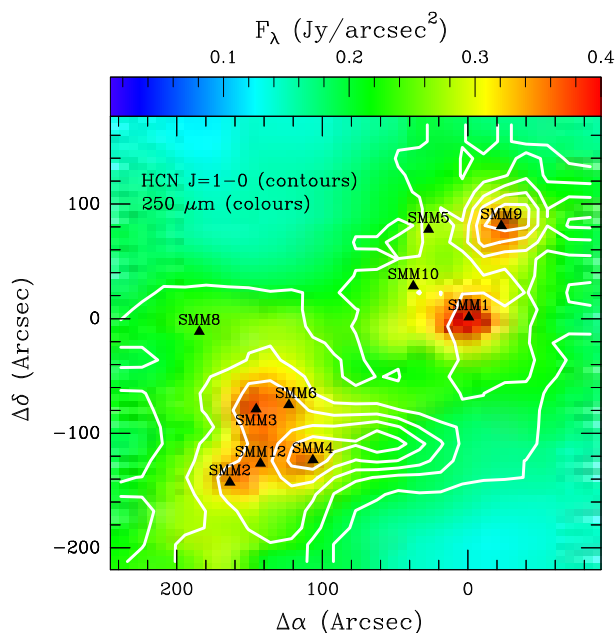


Fig. 1: EMIR map of HCN 1-0 (contours) on top of the continuum emission at $250\ \mu\text{m}$ from *Herschel*/SPIRE. The HCN contours start at $0.4\ \text{K km s}^{-1}$ and are drawn in steps of $4\ \text{K km s}^{-1}$. The properties of protostars are shown in Table 1.

In the environment of low-mass protostars, the possible role of UV radiation was detected in narrow ^{12}CO 6-5 lines spatially associated with outflow cavities in HH 46 (van Kempen et al. 2009b). Firm detection of $[\text{C I}]$ 2-1 at the tip of the HH 46 jet and the lack of CO was attributed to the presence of dissociative bow shock capable of producing extra UV photons (Neufeld & Dalgarno 1989). Their transport on $\sim 1000\ \text{AU}$ scales is facilitated by the low densities and scattering in the outflow cavities (Spaans et al. 1995). Similar signatures of UV radiation were observed in a dedicated APEX-CHAMP⁺ survey of ~ 20 protostars (Yildiz et al. 2012, 2015).

Far-infrared observations with *Herschel* provided access to CO lines with J_u up to 49, and resulted in the detection of new hydrides, e.g. OH^+ (Wyrowski et al. 2010) and H_2O^+ (Ossenkopf et al. 2010). As part of the ‘Water in star-forming regions with *Herschel*’ (WISH, van Dishoeck et al. 2011) key program, a statistically significant sample of low-mass protostars was surveyed with the Heterodyne Instrument for the Far-Infrared (HIFI, de Graauw et al. 2010) and the Photodetector Array Camera and Spectrometer (PACS, Poglitsch et al. 2010). Among the key findings are: (i) ubiquitous gas at temperature of $\sim 300\ \text{K}$ with molecular signatures resembling shocks (Herczeg et al. 2012; Goicoechea et al. 2012; Karska et al. 2013, 2018); (ii) a consistently low abundance of H_2O of $\sim 10^{-6}$ (Kristensen et al. 2017); (iii) high abundances of the products of H_2O photodissociation and other hydrides, in particular OH (Wampfler et al. 2013; Benz et al. 2016); (iv) velocity-resolved components in H_2O profiles arising close to the protostar, at the positions of hydrides (Kristensen et al. 2013); (v) ratios of $\text{H}_2\text{O}/\text{OH}$ and CO/OH consistent with UV-irradiated shock models (Karska et al. 2018). These results confirm the presence of UV photons in the immediate surroundings of low-mass protostars.

In this paper, we analyse large-scale maps in HCN and CN as alternative tracers of UV photodissociation toward Serpens, a low-mass star-forming region, in order to address the following

questions: What is the morphology and spatial extent of the regions affected by UV radiation? Are there systematic differences in the ratios of CN and HCN between protostar and outflow positions? Does chemical models validate the utility of this ratio as a tracer of UV-irradiated gas in low-mass star-forming regions? What is the typical strength of UV radiation in Serpens determined from CN and HCN, and how it compares to the results from *Herschel*?

The paper is organized as follows: Section 2 describes the Serpens Main region and its protostars, the observations and data reduction. Section 3 show the submillimetre maps and the line profiles at selected positions. Section 4 shows the determination of molecular column densities and their comparisons to the chemical model. Section 5 discusses the results in the context of complementary studies and Section 6 presents the summary and conclusions.

2. Source sample and observations

2.1. Serpens as a low-mass star-formation site

The Serpens is a well-studied low-mass star-forming region located at the distance of $436 \pm 9\ \text{pc}$ (Ortiz-León et al. 2017). The identification and classification of young stellar objects (YSOs) was done in the region as part of the *Spitzer* ‘From Molecular Cores to Planet-forming Disks’ (c2d) survey (Harvey et al. 2007; Enoch et al. 2009; Evans et al. 2009; Dunham et al. 2015). Submillimetre sources were studied using continuum observations at $12, 25, 60, 100\ \mu\text{m}$ (Hurt & Barsony 1996), $800, 1100, 1300$ and $2000\ \mu\text{m}$ (Casali et al. 1993) and $3\ \text{mm}$ (Testi & Sargent 1998). The outflow activity in the Serpens Main was characterized using CO 2-1 (Davis et al. 1999), and more recently with CO 3-2 and CO 6-5 for a subsample of sources (Graves et al. 2010, Dionatos et al. 2010, Yıldız et al. 2015). Ser SMM1, SMM3 and SMM4 were observed with *Herschel* as part of the WISH and ‘Dust, Ice, and Gas in Time’ (DIGIT, Green et al. 2013, 2016; Yang et al. 2018) programs.

Figure 1 shows the continuum map at $250\ \mu\text{m}$ corresponding to the region we observed with IRAM 30 m. The map was obtained with the *Herschel* Spectral and Photometric Imaging REceiver (SPIRE; Griffin et al. 2010) as part of the ‘*Herschel* Gould Belt Survey project’ (André et al. 2010).

For the purpose of our analysis, we re-calculated spectral energy distributions (SEDs) for all protostars in the region using the continuum measurements at $70, 160, 250, 350$ and $500\ \mu\text{m}$ from PACS and SPIRE covering the peak of the SEDs and following the procedures outlined in (André et al. 2010, Kirk et al. 2013, Könyves et al. 2015). **Figure A.1 and Table A.1 present the SEDs of the protostars and provide flux densities at each wavelength.** Table 1 shows the bolometric luminosities and temperatures, and the classification of the sources based on Evans et al. (2009).

2.2. Observations and data reduction

The observations at IRAM 30 m were performed between 14 and 17 July 2009 as part of the project ‘HCN/CN as UV-tracers in YSO envelope-outflow interfaces’ (PI: L. Kristensen). The Eight Mixer Receiver (EMIR) bands E090 and E150 covering the frequency ranges $73\text{--}117\ \text{GHz}$ and $125\text{--}184\ \text{GHz}$ were used to observe HCN 1-0, CN 1-0 and CS 3-2. The broad frequency ranges of EMIR facilitated additional detections of C^{34}S 3-2, H^{13}CN 1-0 and H^{13}CN 2-1. The backend was the Versatile Spectrometer Array (VESPA) autocorrelator and the $1\ \text{MHz}$ filter-

Table 1: Properties of targeted protostars in Serpens

| Source | R.A. (J2000.0) | Decl. (J2000.0) | T_{bol} (K) | L_{bol} (L_{\odot}) | Class | Other names |
|--------|-------------------|--------------------|-------------------------|-------------------------------------|-------|---|
| SMM 1 | 18 29 50.0 | +01 15 20.3 | 35 | 78.7 | 0 | Ser-emb6, FIRS1, EC41, Bolo23 |
| SMM 2 | 18 30 00.5 | +01 12 57.8 | 31 | 4.1 | 0 | Ser-emb4, Bolo28 |
| SMM 3 | 18 29 59.6 | +01 13 59.2 | 35 | 6.9 | 0 | Ser-emb26, Bolo26 |
| SMM 4 | 18 29 57.0 | +01 13 11.3 | 77 | 4.4 | I | Ser-emb22, Bolo25 |
| SMM 5 | 18 29 51.4 | +01 16 38.3 | 151 | 3.7 | I | Ser-emb21, EC53, WMW24, Bolo22 |
| SMM 6 | 18 29 57.8 | +01 14 05.3 | 532 | 43.1 | I | Ser-emb30, EC90, WMW35, SVS20S, Bolo 28 |
| SMM 8 | 18 30 01.9 | +01 15 09.2 | 15 | 0.2 | 0 | Bolo30 |
| SMM 9 | 18 29 48.3 | +01 16 42.7 | 35 | 10.3 | 0 | Ser-emb8, ISO241, WMW23, Bolo22 |
| SMM 10 | 18 29 52.3 | +01 15 48.8 | 83 | 6.2 | I | Ser-emb12, WMW21, Bolo 23 |
| SMM 12 | 18 29 59.1 | +01 13 14.3 | 97 | 5.7 | I | Ser-emb19, Bolo28 |

Notes. Source coordinates are adopted from Suresh et al. (2016) except for Ser SMM8, which position is listed in Lee et al. (2014). Calculation of T_{bol} and L_{bol} is presented in Appendix 6.

Table 2: Catalog of the observed molecular lines with IRAM and APEX

| Mol. | Trans. | E_u/k_B (K) | Freq. (GHz) | Telescope | Beam size ($''$) | Efficiency η_{MB} |
|--------------------|--------|------------------|----------------|-------------|-----------------------|----------------------------------|
| HCN | 1-0 | 4.25 | 88.631847 | IRAM-EMIR | 28 | 0.81 |
| H ¹³ CN | 1-0 | 4.14 | 86.340184 | IRAM-EMIR | 29 | 0.81 |
| | 2-1 | 12.43 | 172.677881 | IRAM-EMIR | 14 | 0.68 |
| CN | 1-0 | 5.45 | 113.490985 | IRAM-EMIR | 22 | 0.78 |
| C ³⁴ S | 3-2 | 13.9 | 144.617109 | IRAM-EMIR | 16 | 0.74 |
| CS | 3-2 | 14.1 | 146.969029 | IRAM-EMIR | 16 | 0.74 |
| ¹² CO | 6-5 | 116.2 | 691.473076 | APEX-CHAMP+ | 9 | 0.48 |

Notes. Molecular data adopted from the Leiden Atomic and Molecular Database (LAMDA, Schöier et al. 2005) and the JPL database (Pickett et al. 1998).

bank reaching the spectral resolution of 39 kHz (E150 band) and 78 kHz (E090 band). Table 2 shows the full list of molecular transitions observed with EMIR with respective beam sizes and the main beam efficiencies (η_{MB}) used to convert antenna temperatures to the main beam temperatures (T_{MB}).

The OTF mode was used to obtain two $5' \times 5'$ maps centred at $(\alpha_{\text{J2000}}, \delta_{\text{J2000}}) = 18^{\text{h}}29^{\text{m}}49.6^{\text{s}}, +01^{\circ}15'20.5''$, and $18^{\text{h}}29^{\text{m}}56.6^{\text{s}}, +01^{\circ}14'00.3''$. The merging and data reduction were carried out with the CLASS package within GILDAS¹. For the sake of analysis, the EMIR spectra were baseline-corrected and resampled to a resolution of 0.5 km/s. The rms of extracted spectra varies from 0.024 K to 0.125 K. Figure 2 shows the size and extent of the maps after the merging of two datasets and beam convolution.

The CHAMP+ dual-beam heterodyne receiver on the Atacama Pathfinder Experiment (APEX) telescope used for CO 6-5 observations at 691.5 GHz was originally presented in Yıldız et al. (2015). The observations were performed on 16 June 2009 using position-switching in on-the-fly mapping mode resulting in maps covering $340'' \times 340''$. The Fast Fourier Transform Spectrometer (FFTS) was used as the backend with a resolution of 0.079 km s^{-1} (Klein et al. 2006). Typical value of rms is $\sim 0.018 \text{ K}$. Similarly, observations of the Ser SMM1 protostar in C¹⁸O were obtained with the APEX/CHAMP+ on 23 October 2009. The data reduction and analysis were performed in a similar way to the IRAM observations using the CLASS software.

3. Results

In the following sections, we present IRAM 30 m maps and line profiles providing complementary information about the emission from protostars and their outflows, and large-scale cloud emission. Differences in spatial extent reflect the range of gas and dust distributions, and associated physical conditions and processes. We calculate ratios of various transitions to indicate species tracing similar physical components, the gas temperature, and line opacities.

3.1. Spatial extent of line emission

Figure 2 shows the line emission associated with protostars and their outflows in HCN, CN and CS lines obtained with EMIR on IRAM 30 m and CO with CHAMP+ on APEX. The emission in HCN and CN is the sum of all hyperfine components detected in the spectra (see Figure 3). Maps in additional transitions are presented in Appendix B.

HCN 1-0 emission is associated with clusters of protostars in the south-east and north-west parts of the map where dust emission at $250 \mu\text{m}$ is also detected (Figure 1). The emission peaks are the strongest at the positions of Ser SMM4 and SMM9 protostars and their outflows, and significantly weaker at Ser SMM1 and SMM3. Qualitatively, the pattern of emission in HCN is similar to the CO 6-5 - the well-established outflow tracer (Figure 2; bottom right panel). This results is in agreement with previous surveys of HCN in low-mass protostars (Bachiller et al. 2001; Walker-Smith et al. 2014). Any differences between HCN and CO likely stem from the higher critical density of the HCN 1-0 ($\sim 10^6 \text{ cm}^{-2}$), its lower upper energy level (see Table 2), and its

¹ See <http://www.iram.fr/IRAMFR/GILDAS>

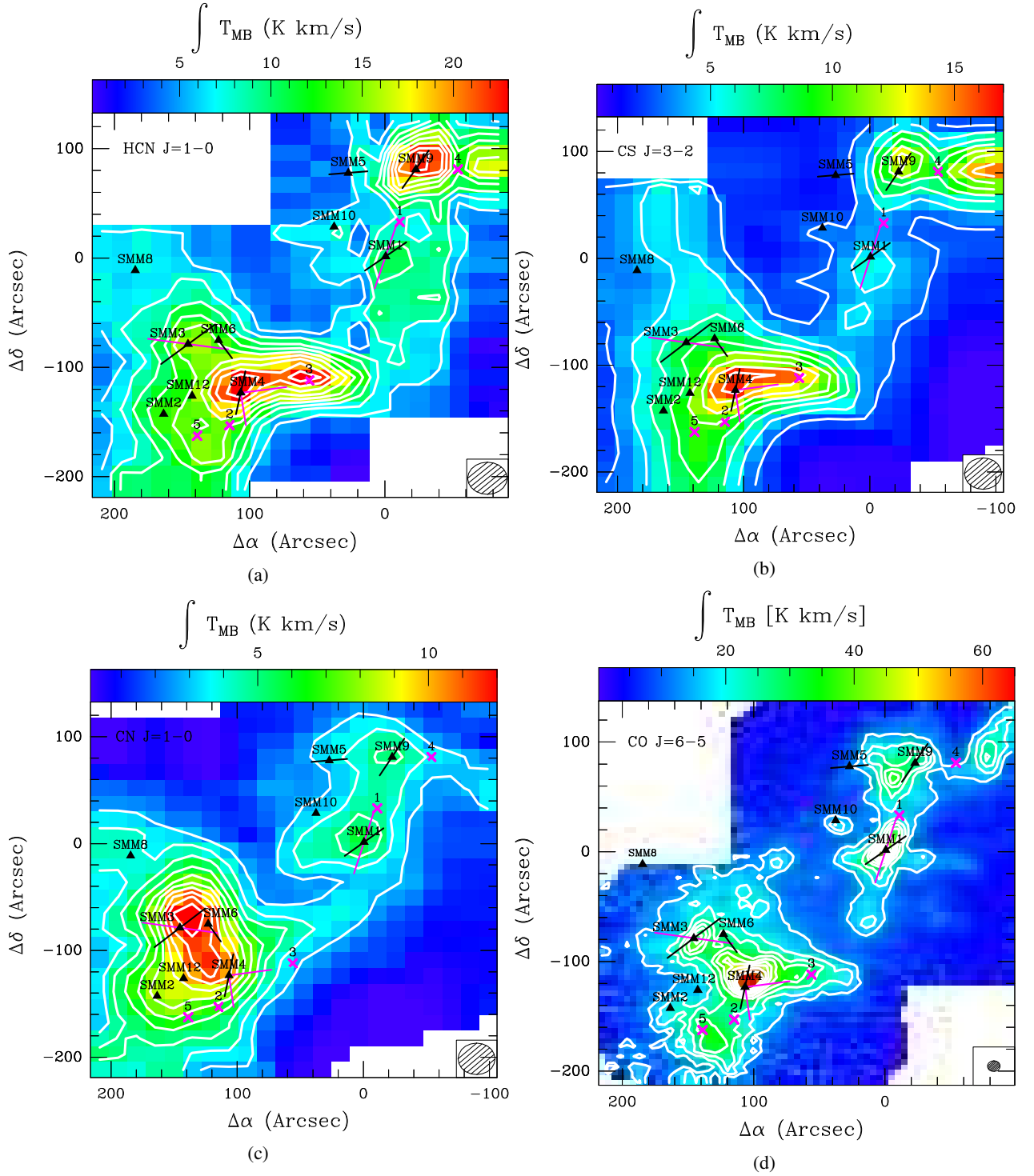


Fig. 2: Integrated intensity maps of the HCN 1-0 (upper left panel), CS 3-2 (upper right panel), CN 1-0 (bottom left panel) and CO 6-5 (bottom right panel) toward Serpens star-forming region with IRAM 30 m. Black triangles show the positions of protostars (see Table 1) and magenta crosses show the outflow positions selected for analysis (see Table 3). Solid lines show outflow directions from CO 6-5 (black; Yıldız et al. 2015) and CO 3-2 (magenta; Dionatos et al. 2010). The center of the maps (0,0) corresponds to $(\alpha, \delta) = 18^{\text{h}}29^{\text{m}}46.6^{\text{s}}, 01^{\circ}18'20.5''$. Contour levels start at 30σ for HCN and CN and increase every 10σ . For CS and CO, the first contours are at 10σ and 70σ levels, and the steps are 5σ and 30σ , respectively.

significantly easier photodissociation due to UV photons than CO (see Section 5).

CS 3-2 emission shows a very similar spatial distribution to HCN 1-0 and CO 6-5, with most prominent structures associated with Ser SMM4. Some differences are seen mostly in the

surrounding of Ser SMM9, where CS emission is substantially weaker at the Ser SMM9 position than in Ser SMM4, in contrast to HCN which shows similar line strengths towards both protostars. Additionally, CS shows a relatively strong emission to the west of Ser SMM9, which coincides with the outflow from that

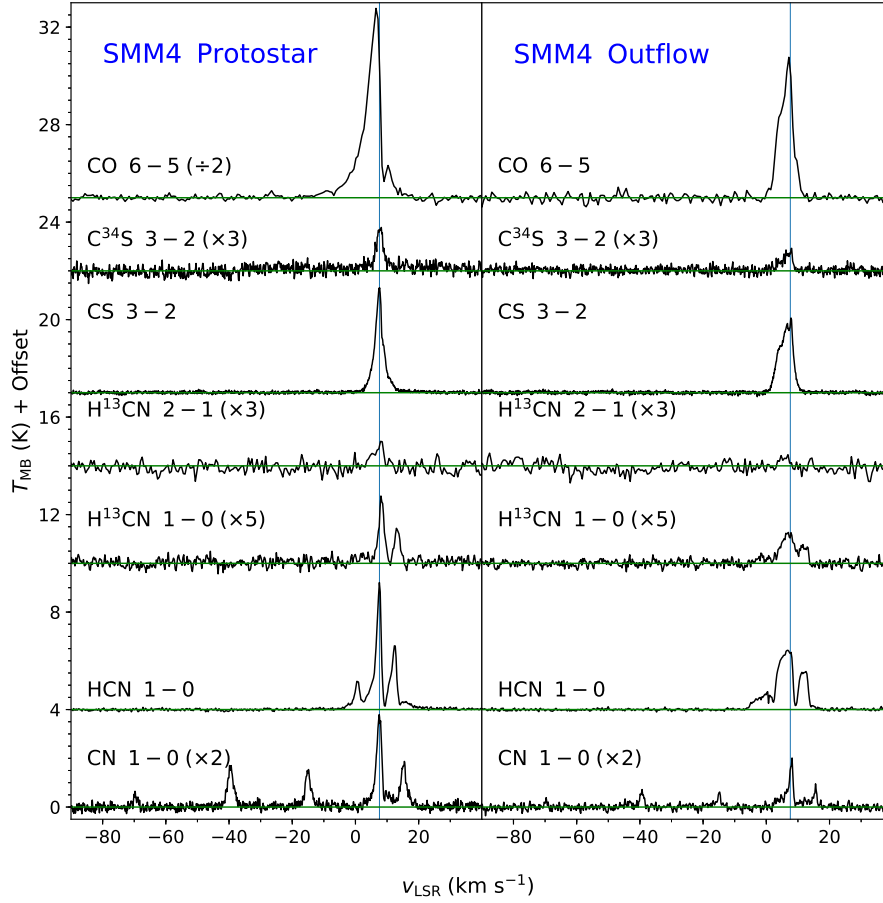


Fig. 3: Line profiles of CO 6-5, $C^{34}S$ 3-2, CS 3-2, $H^{13}CN$ 2-1, $H^{13}CN$ 1-0, HCN 1-0 and CN 1-0 lines at the protostar position Ser SMM4 (left) and the associated outflow position nr 3 (right). Spectra of CO 6-5, $C^{34}S$ 3-2, $H^{13}CN$ 2-1, $H^{13}CN$ and CN are scaled in flux by a factor of 0.5, 3, 3, 5 and 2, respectively.

protostar. The differences may result from CS tracing warmer, yet lower-density gas ($n_{\text{crit}} \sim 10^5 \text{ cm}^{-3}$).

In contrast to HCN and CS, CN 1-0 emission is associated more closely with the positions of protostars and the continuum peaks at $250 \mu\text{m}$, and not the outflows (Figures 1 and 2). The emission is the strongest at Ser SMM4, SMM3, and SMM6, and the region in between these three protostars. The differences in spatial extent between CN and the outflow tracers suggest a different physical origin (see Section 5.1).

3.2. Detection rates and line profiles

To explore gas properties in Serpens, we selected 10 protostellar positions and 5 outflow positions for more in-depth analysis. **The later are selected considering their vicinity to the previously known outflows and emission peaks on the maps in Figure 2.** Figure 3 shows line profiles of targeted species and transitions toward Ser SMM4 and its outflow. Appendix C shows the line profiles in the remaining positions.

All targeted species and their isotopologues are detected in each position towards the protostars in Serpens, except the $H^{13}CN$ 2-1 which is detected only in Ser SMM4 and Ser SMM9. Similarly, emission in the outflow positions is always detected in HCN, CS, CN and CO. Considering the targeted lines isotopologues, detections are seen in $C^{34}S$ 3-2, $H^{13}CN$ 1-0, but not in

$H^{13}CN$ 2-1. In case of HCN and CN, up to 3 and 5 components are detected as the result of the hyperfine splitting, respectively.

The line shapes at both protostar and outflow positions show a relatively broad profiles, with outflow wings in CS extending of 13.6 km s^{-1} and 9.8 km s^{-1} at Ser SMM4 source and outflow, respectively (Figure 3). Clearly, the beam sizes of IRAM encompass a substantial amount of outflow emission even at the protostar position.

In order to quantify the emission in the line wings, we use the line profile of $C^{18}O$ 6-5 for Ser SMM1, which is a good envelope tracer (Arce & Sargent 2006). The profile extends from 7.8 to 9.4 km s^{-1} - the velocity ranges we exclude for the intensity integration of our line profiles. The outer velocity ranges for each of the profiles are calculated for each line separately based on the measured rms and the 2σ signal. Appendix D shows the calculated intensities for all selected positions.

In the case of Ser SMM4 (Figure 3), the emission in the line wings of CS 3-2 is 61% of the total profile in the protostar position and 72% in the outflow position. Similar characteristics is seen in HCN line wings (48% and 68%, respectively). In contrast, CN 1-0 is detected mostly at source velocity, with only 40% of emission in the line wings. Among all 15 positions, exceptionally broad line wings in HCN and CS are detected in the Ser SMM1, Ser SMM9 and Ser SMM10 protostar positions and outflow positions nr 1, 4, and 5, exceeding 70% of the total profile in HCN and 58% in CS.

Table 3: Molecular line ratios of the fully integrated line profile and the line wings

| Source | CN / HCN | | CS / CO | | HCN / CO | | HCN / H ¹³ CN | | CS / C ³⁴ S | H ¹³ CN 2-1/1-0 |
|---------------------|----------|------------|---------|------------|----------|------------|--------------------------|------------|------------------------|----------------------------|
| | Full | Line wings | Full | Line wings | Full | Line wings | Full | Line wings | Full | Full |
| Protostar positions | | | | | | | | | | |
| Ser SMM1 | 0.61 | 0.40 | 0.08 | 0.05 | 0.14 | 0.10 | 6.51 | 12.45 | 4.66 | - |
| Ser SMM2 | 0.65 | 0.53 | 0.38 | 0.23 | 0.58 | 0.35 | 8.74 | 22.28 | 9.98 | - |
| Ser SMM3 | 0.85 | 0.57 | 0.16 | 0.10 | 0.27 | 0.10 | 25.99 | 42.90 | 16.50 | - |
| Ser SMM4 | 0.47 | 0.40 | 0.16 | 0.12 | 0.23 | 0.13 | 13.43 | 14.91 | 9.88 | 1.98 |
| Ser SMM5 | 0.67 | 0.31 | 0.19 | 0.09 | 0.31 | 0.17 | 5.26 | - | 7.95 | - |
| Ser SMM6 | 0.81 | 0.55 | 0.29 | 0.19 | 0.44 | 0.14 | 15.10 | 17.39 | 11.19 | - |
| Ser SMM8 | 0.43 | 0.27 | - | - | - | - | 49.39 | 117.2 | 17.57 | - |
| Ser SMM9 | 0.24 | 0.11 | 0.34 | 0.30 | 0.57 | 0.49 | 8.73 | 16.33 | 6.78 | 1.31 |
| Ser SMM10 | 0.41 | 0.15 | 0.14 | 0.09 | 0.29 | 0.23 | 7.00 | 31.11 | 9.12 | - |
| Ser SMM12 | 0.71 | 0.63 | 0.57 | 0.40 | 0.82 | 0.49 | 8.84 | 10.82 | 17.70 | - |
| Outflow positions | | | | | | | | | | |
| 1 (-11.00,33.00) | 0.58 | 0.24 | 0.24 | 0.15 | 0.43 | 0.31 | 9.87 | - | 4.16 | - |
| 2 (114.86,-153.00) | 0.51 | 0.47 | 0.35 | 0.24 | 0.47 | 0.27 | 13.48 | 27.12 | 10.71 | - |
| 3 (56.00,-112.00) | 0.13 | 0.03 | 0.54 | 0.56 | 0.74 | 0.72 | 11.92 | 12.29 | 15.57 | - |
| 4 (-54.00,81.00) | 0.25 | 0.13 | 0.63 | 0.54 | 0.97 | 0.84 | 8.38 | 12.12 | 8.90 | - |
| 5 (138.86,-162.60) | 0.56 | 0.49 | 0.26 | 0.18 | 0.36 | 0.21 | 9.05 | 11.52 | 9.76 | - |

Notes. Sources in the upper part of the table refer to the positions of protostars within the IRAM maps (Figure 1 and 2), positions in the lower part refer to selected outflow positions on the same maps. Coordinates of the outflow positions refer to the centre of the map (J2000 RA 18:29:49.6 and DEC 01:15:20.5.)

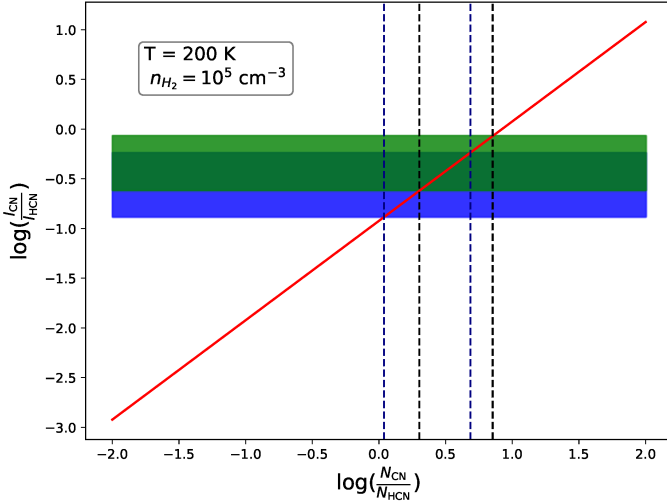


Fig. 4: The ratio of CN and HCN column densities obtained with RADEX for $n_{\text{H}} = 10^5 \text{ cm}^{-3}$ and $T_{\text{kin}} = 200 \text{ K}$ (red line). The observed line intensity ratio is shown as a rectangle, with light green colour corresponding to the values observed at the protostar position, blue colour for the outflow positions and dark green colour for both regions. Column density ranges are marked with black and navy dashed lines for protostars and outflow positions, respectively.

The shapes of line profiles clearly indicate that the emission in various species is detected in different physical components of the protostellar systems. For the forthcoming analysis, we will consider the emission in the line wings alone and in the fully integrated profiles separately.

Table 4: Model-dependent column density ratios of CN and HCN

| n_{H_2} (cm^{-3}) | T_{kin} (K) | $\log_{10}(\text{N}(\text{CN})/\text{N}(\text{HCN}))$ protostars | $\log_{10}(\text{N}(\text{CN})/\text{N}(\text{HCN}))$ outflows |
|--|-------------------------|---|---|
| 10^4 | 30 | 0.24-0.79 | -0.02-0.63 |
| 10^4 | 75 | 0.16-0.71 | -0.10-0.55 |
| 10^4 | 200 | 0.12-0.67 | -0.14-0.51 |
| 10^5 | 30 | 0.28-0.83 | 0.016-0.67 |
| 10^5 | 75 | 0.27-0.82 | 0.00-0.65 |
| 10^5 | 200 | 0.30-0.85 | 0.04-0.69 |
| 10^6 | 30 | 0.38-0.92 | 0.10-0.75 |
| 10^6 | 75 | 0.43-0.98 | 0.16-0.81 |
| 10^6 | 200 | 0.50-1.05 | 0.23-0.88 |

3.3. Line ratios

Table 3 shows the molecular line ratios at protostar and outflow positions in Serpens calculated separately for the fully integrated profiles and for the line wings. Here, we will discuss the results for (i) the ratios of different isotopologues, informing about the line opacities, (ii) the ratio of two transitions of H¹³CN, indicating gas temperature, (iii) ratios of different species, reflecting their relative abundances.

3.3.1. Ratios of different isotopologues

The line ratio of the same transition of two isotopologues can be used as a line opacity tracer of the more abundant species, assuming that the emission in the other isotopologue is optically thin. We adopt a standard method described in Goldsmith et al. (1984) to determine the line opacities of HCN 1-0 and CS 3-2 lines, both in the protostar and outflow positions. We assume that both isotopologues arise from the same physical region, described by the excitation temperature, T_{exc} , and in local thermodynamic equilibrium (LTE). Using Equation 1, we obtain the values of 0.3-5.7 and 0.3-4.8 for the fully-integrated line profiles

of HCN and CS with their isotopologues respectively.

$$\frac{T_{\text{HCN}}}{T_{\text{H}^{13}\text{CN}}} = \frac{X[\text{HCN}]}{X[\text{H}^{13}\text{CN}]} \frac{1 - \exp(-\tau_{\text{HCN}})}{\tau_{\text{HCN}}} \quad (1)$$

In this expression τ_{HCN} is the optical depth of HCN, X_i refers to the abundance of an isotopologue and T_i to the antenna temperatures. For comparison, the expected ratio in case of optically thin emission is 30 and 20 for the ratio of HCN and H^{13}CN (Daniel et al. 2013), and the ratio of CS and C^{34}S (Tercero et al. 2010). Thus, the emission in both species is optically thick when the entire profile is considered. In contrast, the ratio of HCN and H^{13}CN in the line wings is in the range from about 10 to 40, with the exception of Ser SMM8 **located at the map edge**, corresponding to optical depths of 0.6–2.6 (see Table 3). Similarly, the line ratio of CS and C^{34}S is 5–20, corresponding to $\tau \approx 0.8 - 2.6$. Thus, high-velocity emission of HCN and CS in the outflow wings at both protostar and outflow positions is basically optically thin.

An alternative method of calculating optical depth uses the ratios of various hyperfine split components, yet for HCN this method shows considerable anomalies (Loughnane et al. 2012). Therefore, we apply it only for the three strongest components of CN, $F=3/2 \rightarrow 1/2$, $F=5/2 \rightarrow 3/2$, $F=1/2 \rightarrow 1/2$, which optically thin ratios are 0.1235:0.3333:0.0988 (Skatrud et al. 1983). The optical depths of observed emission vary from 0.4 to 1.6 in protostar position and from 0.2 to 1.0 for outflow positions is consistent with the values obtained for HCN and CS. Qualitatively, they are also in agreement with simple calculations using 1D non-LTE radiative-transfer code RADEX (van der Tak et al. 2007). Here, adopting hydrogen density of 10^5 cm^{-3} and kinetic temperature of the gas of 50 K (Mottram et al. 2014), results in the optical depths of 4.4 for HCN 1-0 and 2.1 for CS 3-2, assuming column densities of $3 \times 10^{14} \text{ cm}^{-2}$ for HCN and $5 \times 10^{13} \text{ cm}^{-2}$ for CS.

3.3.2. The H^{13}CN 2-1/1-0 ratio

The H^{13}CN 2-1 emission is detected only in Ser SMM4 and Ser SMM9, with the ratio of 1.98 and 1.31, respectively. Using two transitions of the same molecule, the excitation temperature is calculated using Equation 2, where E_i refers to the energy of a level and n_i refers to population of upper and lower level.

$$T_{\text{ex}} = \frac{E_u - E_l}{k \ln \frac{n_u}{n_l}} \quad (2)$$

The excitation temperature is 2.43 K and 2.77 K for Ser SMM4 and Ser SMM9, respectively. These values are much lower than expected in envelopes and outflows of low-mass protostars. In particular, gas temperatures in Ser SMM1, 3, and 4 calculated using multiple lines of ^{13}CO and C^{18}O are 40–60 K and ^{12}CO are 70–100 (Yıldız et al. 2012, 2013). The disagreement with our observations likely results from the low signal-to-noise of the H^{13}CN 2-1 line.

3.3.3. Ratios of different species

The median value of the CN and HCN ratio at the protostars positions is 0.63 ± 0.19 . Taking into account the emission in wings only the ratio is lower: 0.40 ± 0.18 . The ratio calculated for the outflow positions equals 0.51 ± 0.20 and 0.24 ± 0.20 (derived from full profile and wings respectively). The CN and HCN ratio varies between 0.13 at the Outflow 3 to 0.85 at the Ser SMM3.

There is no significant dependence between the CN and HCN ratio and the evolutionary stage of a source. The ratio for the Class 0 protostars is 0.61 ± 0.23 and for the Class I protostars is 0.67 ± 0.17 . Similarly, the median for the wings emission is 0.40 ± 0.19 irrespectively of the class of protostars.

4. Analysis

In this section, we calculate column densities of the molecules with the radiative-code RADEX and compare them to the results from the chemical-code Nahoon, run for a set of gas temperatures, densities and UV radiation fields.

4.1. Column densities of molecules from observations

In case of optically thin lines and LTE conditions, the column density of the upper level of a given molecule, N_u , can be calculated using Equation 3, where β is a constant equal to 1937 cm^{-2} , W is the integrated intensity of the emission line ($\int T_{\text{mb}} dV$), and ν is a transition frequency between an upper and a lower level expressed in GHz.

In order to calculate the total column density of a given molecule, we adopt a gas temperature of 75 K (see Section 3.3.2). Equation 4 takes into account the temperature-dependent partition function $Q(T)$ for a given molecule, and the upper level energies (E_u) and level degeneracies (g_u); k_B is the Boltzmann constant. Appendix E shows column densities obtained for all molecules, both at the protostars and the outflow positions.

$$N_u = \beta \frac{\nu W}{A} \quad (3)$$

$$N_{\text{tot}} = Q(T_{\text{exc}}) \exp\left(\frac{E_u}{k_B T_{\text{exc}}}\right) \frac{N_u}{g_u} \quad (4)$$

Because of the optical thickness of HCN (Section 3.3.1), we also employ the non-LTE radiative transfer code RADEX to obtain independent determinations of the column densities. In order to mimic the optically thin case, for the calculations we adopt the HCN column density of 10^8 cm^{-2} . We vary the column density of CN from 10^6 to 10^{10} cm^{-2} . The typical physical conditions of the gas in low-mass star forming regions are: number densities, n_{H} of the order of 10^4 – 10^6 cm^{-3} and kinetic temperature T_{kin} of 30–200 K (Mottram et al. 2014). Table 4 shows the ratios of the calculated column densities of CN and HCN for these different sets of parameters, and assuming a line width of 1.0 km s^{-1} , separately for protostars and outflows positions.

The models are a mean to translate the observed line ratios of CN and HCN into column densities ratios. Figure 4 shows the model calculated for the density of 10^5 cm^{-3} and kinetic temperature of 200 K, typical for outflows in low-mass protostars (van Kempen et al. 2009b, Yıldız et al. 2015). Similar models are calculated for other sets of temperatures and densities, and the determined scaling factors between the intensity and column density ratios show a very weak dependence on the adopted physical parameters (Appendix E). The observed line intensity ratio (full profile) in logarithm ranges from -0.62 to -0.07 and from -0.87 to -0.24 for protostars and outflow positions, respectively. The corresponding column density ratio is in the range 0.12 to 1.05 and -0.14 to 0.88. The resulting column density ratios of CN and HCN are in order of 1–10.

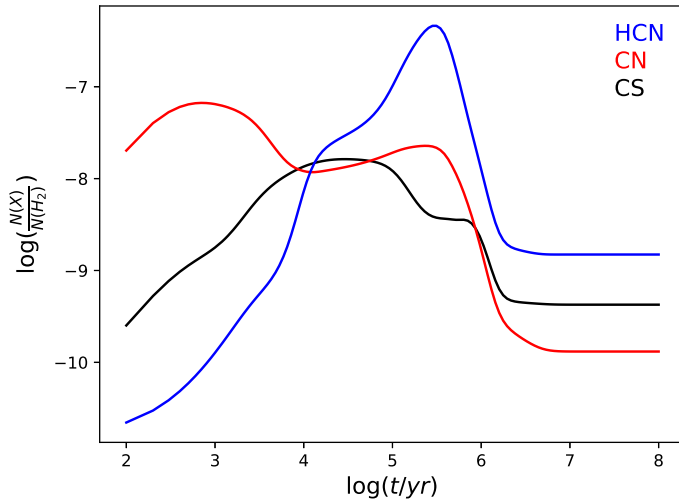


Fig. 5: Time evolution of CN (red line), HCN (blue line) and CS (black line) abundances obtained with Nahoon astrochemical code with initial parameters of $n_H = 10^4 \text{ cm}^{-3}$, $T = 10 \text{ K}$, $A_V = 5 \text{ mag}$. **The initial abundances (at $t = 0$) of CN, HCN and CS equal zero.** The assumed cosmic-ray ionization rate is $1.3 \times 10^{17} \text{ s}^{-1}$, dust to gas mass ratio is 0.01, dust grain radius is 10^{-5} cm , grain density is 3 g cm^{-3} .

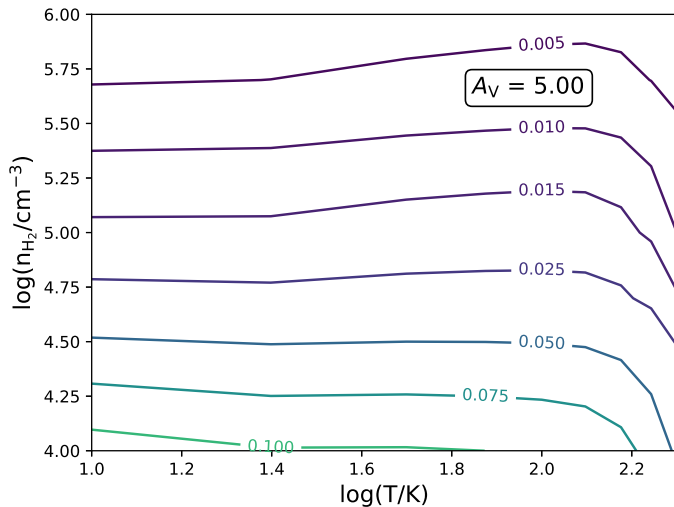


Fig. 6: Contour plot of Nahoon sets of models of CN/HCN abundances ratio with fixed visual extinction $A_V = 5 \text{ mag}$ and 10^7 yr after star formation began in the cloud.

4.2. Theoretical column densities from Nahoon

The Nahoon chemical code is used to calculate theoretical abundances of molecules for a set of physical conditions and UV field strengths; it is a well-known almost purely gas-phase chemical code for astronomical applications (Wakelam et al. 2015).

The Nahoon solver computes the chemical evolution in time including 489 species and 7509 gas-phase and gas-grain reac-

tions based on rate coefficients from the Kinetic Database for Astrochemistry (KIDA) database².

The UV radiation in Nahoon is described through the relation between visual extinction A_V and the photodissociation rate coefficient k (Equation 5). Here, α and γ are the coefficients of photodissociation for HCN, equal to 1.64×10^{-9} and 3.12, respectively (Heays et al. 2017).

$$k = \alpha e^{-\gamma A_V} \quad (5)$$

In our analysis we used the latest version of Nahoon code (Nahoon_kida.uva.2014). The evolution of the chemical network starts at the time of a dense cloud formation. Figure 5 shows a model corresponding to a typical dense cloud with temperature of 10 K and hydrogen total density of $n_H = 10^4 \text{ cm}^{-3}$. The chemical composition of the CN, HCN and CS molecules becomes stable after 10^7 yr ; the HCN abundance is higher than that of CN. Assuming that star-formation begins at $t = 10^6 \text{ yr}$ in a dense cloud, we use model abundances for all 489 species at this time as an input data for the forthcoming set of models.

The closest neighbourhood of low-mass protostars is simulated based on the initial abundances of all species from starless cloud modelling. We adopt the cosmic-ray ionization rate of $1.3 \times 10^{17} \text{ s}^{-1}$ (Cravens & Dalgarno 1978). The sets of models are run for the temperature range between 10 and 200 K and the total hydrogen densities from 10^4 cm^{-3} to 10^6 cm^{-3} .

Figure 6 shows the model results assuming visual extinction of 5 mag which corresponds to the lack of UV radiation. In that case, HCN is more abundant than CN by about 2-3 orders of magnitude. The column density ratio of CN and HCN weakly depends on the gas temperature, so we fix the gas temperature at 50K for envelopes of protostars and 200 K for outflows. The model does not include grain chemistry and evaporation of organic material from grains to the gas-phase. However, CN is much more reactive than HCN **what leads to assumption that lack of the grain chemistry cannot increase $N(\text{CN})/N(\text{HCN})$ ratio.**

In the next step, we run the model for a range of visual extinction between -2.5 and 2.5 mag that corresponds to the UV radiation field G_0 of 4×10^{-4} to 2.4×10^3 . Figure 7 show the abundance ratio of CN and HCN as a function of n_H and G_0 for two temperatures. The observed ratios of 1-10 match the calculated ratios in three regimes: for very weak UV fields ($< 10^{-1} G_0$), for the relatively weak UV fields of $10^{-1} - 10^1$ and relatively strong UV fields of $10^2 - 10^3$. **We notice an unusual decrease of C and CO abundances around $0.1-1 G_0$ in the model of $T = 200 \text{ K}$, which probably result in a significant drop of $N(\text{CN})/N(\text{HCN})$ ratio.**

5. Discussion

5.1. Comparison of the spatial extent of CN and HCN

The relative abundance of CN and HCN molecules is a widely used tracer of UV radiation in different astronomical context: reflection nebulae (e.g. Fuente et al. 1995), proto-planetary disks (e.g. Chapillon et al. 2012) or proto-brown dwarfs (e.g. Riaz et al. 2018). CN is a product of photodissociation of HCN with the photodissociation rate of 1.64×10^{-9} . CN has smaller photodissociation rate of 5.19×10^{-10} (Heays et al. 2017), and is therefore less sensitive to photodissociation in comparison to HCN. Since CN and HCN can be photodissociated selectively,

² <http://kida.obs.u-bordeaux1.fr/>

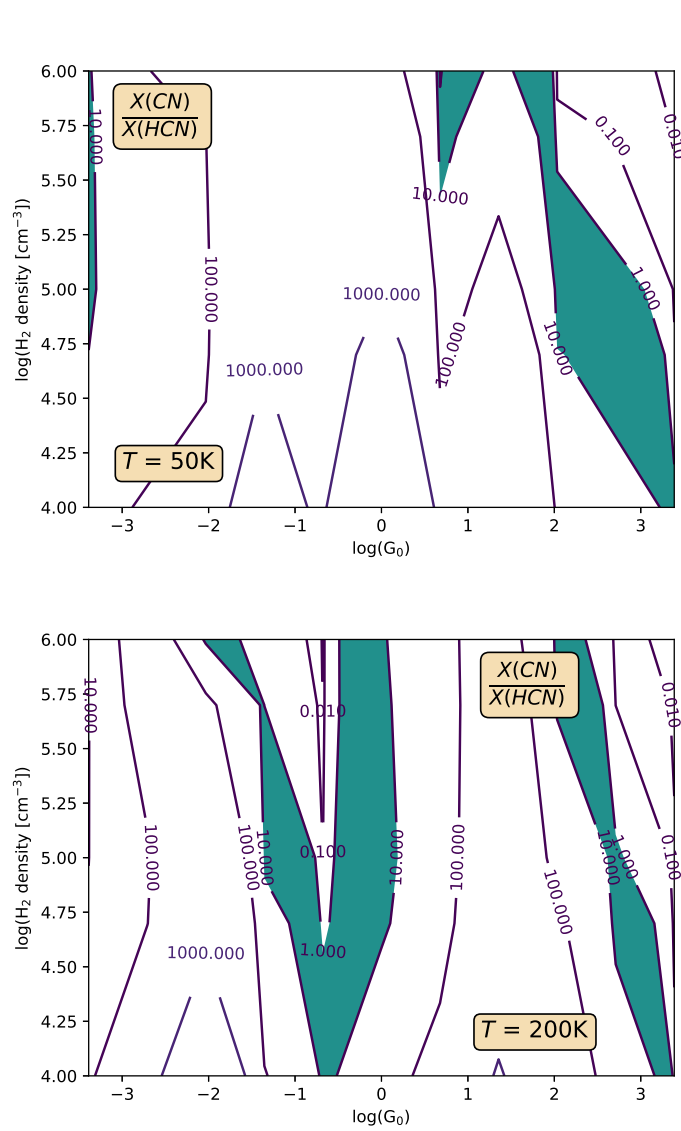


Fig. 7: The column ratio of CN and HCN from Nahoon for a range of hydrogen densities and UV field strengths assuming $T = 200$ K (top) and $T = 50$ K (bottom). The observed column density ratios are shown in green.

the $N(\text{CN})/N(\text{HCN})$ ratio probes regions affected by UV radiation. The ratio is the highest near the source of the UV emission, and decreases with the distance from the source (Fuente et al. 1993).

Figure 8 shows a large-scale map of CN 1-0 and HCN 1-0. The CN 1-0 transition is shifted to the north with respect to the HCN 1-0 emission. It is highly concentrated in the south-east subcluster, while the north-west subcluster is dominated by the HCN. Both molecules show a diffusive ‘bridge’ between the two subclusters. It is connected with Ser SMM4 and Ser SMM1 outflows in HCN, while the CN follows the dust continuum emission. The emission in both molecules is anti-correlated north from Ser SMM6 and west from Ser SMM4 sources.

Both species has been detected in all source positions. CN as a product of HCN photodissociation indicates other properties of low-mass protostars surroundings (Section 4). The highest CN/HCN integrated intensity ratio occurs in Ser SMM6 and Ser SMM3 protostars. On the other hand, Ser SMM9 object is

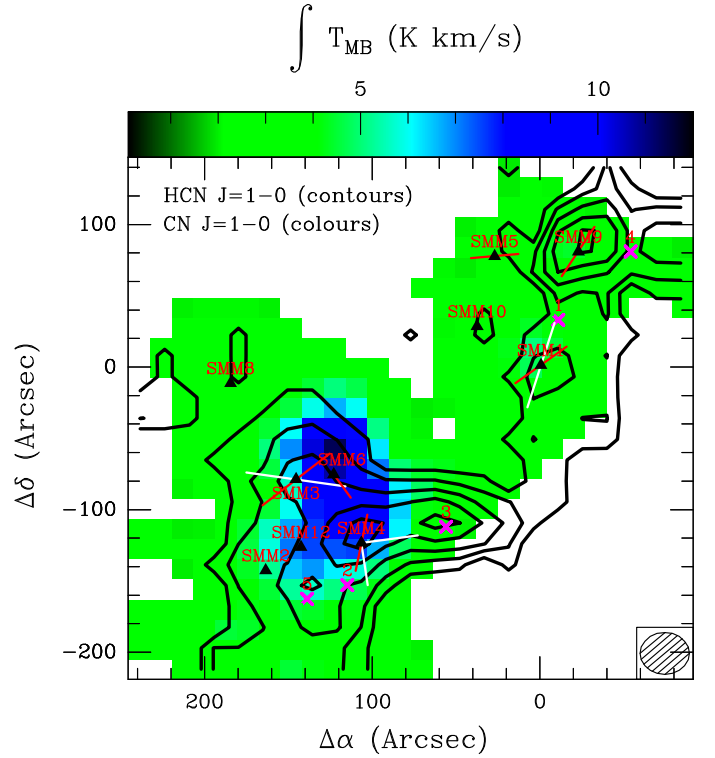


Fig. 8: Map of the intensity ratio of CN 1-0 (colours) and HCN 1-0 (contours) in Serpens. The labels are the same as in Figure 2. Contour levels start at 30σ with the steps of 20σ . The CN emission has been resampled to beam size of HCN in order to compare the same emitting regions.

characterised by very low CN/HCN line ratio. Similarly low CN/HCN ratio is measured in outflow positions no. 3 and 4.

Majority of the sources show firm detection in both molecules (Table 3). However, the variations in line fluxes indicate regions of different properties. The CN/HCN ratio varies between protostars positions, as well as between off-source positions. This parameter does not seem to be correlated with the evolutionary stage of a protostar. All the sources with the highest CN/HCN ratio are located in the south-east subcluster. Ser SMM3 and Ser SMM6 are situated in close neighbourhood, in the area characterised by high emission of CN 1-0 line. At Ser SMM9 and Ser SMM10 protostars the lowest CN/HCN ratio is observed. Both sources are young, Class 0 YSOs. In addition they are separated by ~ 0.095 pc from the other sources.

The same trend can be recognised in the integrated intensity ratio measured in the wings only. The highest ratio is present at the same protostars, although SMM12 shows the highest value in this case. It is located ~ 0.127 pc from the Ser SMM3 and Ser SMM6 protostars, in the area with significantly lower HCN emission. No outflow is known from Ser SMM12. The CO 6-5 line in the neighbourhood of Ser SMM12 does not indicate an outflow either. Extremely low CN and HCN ratio in the wings emission is connected with blue-shifted outflow from Ser SMM4 (outflow position no. 3). In general, this ratio is lower towards outflows in comparison to protostars, indicating that UV radiation is produced in the closest neighbourhood of the protostars. The most prominent emission of the CN line is associated with protostars located in the south-east subcluster, and not related with the evolutionary stage of a source.

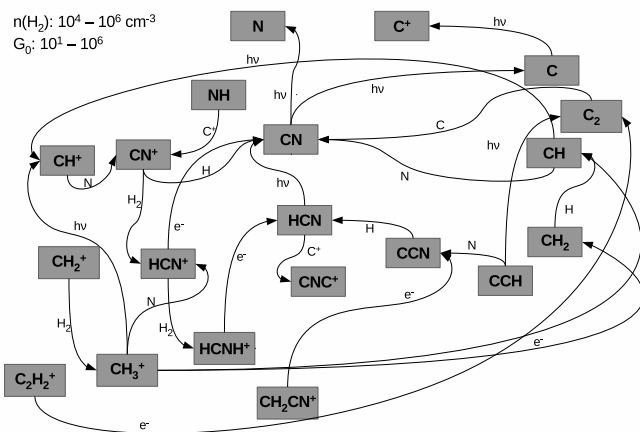


Fig. 9: Reactions network for UV irradiated gas of G_0 UV field higher than $G_0 = 10^1$.

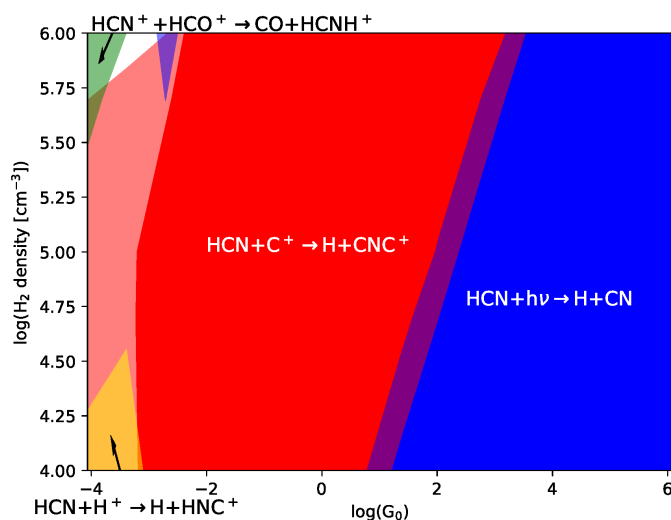


Fig. 10: Dominant reactions of HCN destruction assuming $T = 50$ K. Reactions contributing at least to 50% of the total flux are marked with full colours. Transparent colours correspond to 30%-50% contribution. **HCN + $h\nu$ \rightarrow H + CN reaction is marked with blue colour, $\text{HCN} + \text{C}^+ \rightarrow \text{H} + \text{CNC}^+$ with red colour, $\text{HCN}^+ + \text{HCO}^+ \rightarrow \text{CO} + \text{HCNH}^+$ with green colour and $\text{HCN} + \text{H}^+ \rightarrow \text{H} + \text{HNC}^+$ with yellow colour.**

5.2. UV field strengths in Serpens

In starless, dark clouds HCN is more abundant molecule than CN about an order of magnitude (Pratap et al. 1997). This is in agreement with our model of a starless cloud (Figure 5) at the $10^5 - 10^6$ yr of a cloud evolution. With the further chemical evolution of a starless cloud, the $N(\text{CN})/N(\text{HCN})$ ratio decreases. The measured $N(\text{CN})/N(\text{HCN})$ ratio at protostars and outflow positions varies in the range of 1-10, what leads to conclusion that star-formation initiates processes that change the relative abundances of these two molecules. In the presence of UV radiation, HCN photodissociates into CN molecule and H atom, while CN requires more energetic photons (> 12.4 eV) to be disintegrated (van Dishoeck 1987). This should lead to a higher abundance of CN molecules and an increase of CN/HCN column density ratio. However, our purely

chemical model of the environment of protostars (Figure 7) shows a low CN/HCN ratio even at high UV field. Depending on the assumed temperature, the observed N(CN)/N(HCN) ratio can be reproduced in the UV fields of $G_0 > 10\text{--}100$. Considering UV fields lower than $10^{-3} G_0$, the relative abundance of HCN increases giving the results similar to a starless cloud case.

The N(CN)/N(HCN) ratio can be also shaped by several more factors, including: grain chemistry, evaporation, turbulence, **shelling**, shocks. Both production and destruction of each molecule need to be investigated in order to explain the reason behind HCN abundances being higher than expected. Detailed models of the most dominant reactions for destruction and production of each molecule are presented in Figure 10 and Figure F.1 – Figure F.2 with the assumption of fixed 50 K temperature. Reaction flux is defined as reactants abundances multiplied by reaction rate coefficient. If the accumulated total flux of all reactions contributed in the studied molecules destruction or production processes is greater than 80%, these reactions are taken into consideration as dominant reactions.

The reactions distribution in the parameter space do not strongly depend on hydrogen densities. The strength of UV radiation distinguishes the dominant reactions. Three regimes are defined: with weak ($G_0 < 10^{-1}$), intermediate ($G_0 \sim 10^{-1} - 10^1$) and strong ($G_0 > 10^2$) UV field. The reactions where CN or HCN production or destruction is greater than 30% are listed in Table 5 as well as illustrated in Figure 9, and in Figure F.5- Figure F.4.

In the regime of weak UV radiation fields dominant formation channels of CN and HCN are reactions of nitrogen with hydrocarbons (CH and CH₂ respectively). In denser areas the reaction between an electron and a CNC cation plays a role in the CN formation. In a weakly irradiated environment, atomic elements are more abundant in the neutral state, thus the destruction of CN is mostly dominated by the reactions with neutral oxygen (60-70%) or nitrogen (30% or less). HCN is less reactive, and reaction with neutral atoms are not very efficient in this case. The destruction of HCN is driven by many channels, but reactants are less abundant than neutral atoms. Simultaneous impact of a few different reactions is not as effective as the reaction ruling the CN destruction. Those factors lead to the higher HCN abundances compared to CN.

In the regime of medium UV radiation field more ionized atoms are produced, and concentration of neutral atoms is low. It blocks effective channels of CN destruction, but opens an effective channel of HCN destruction: reaction with abundant C^+ . This reaction results in CNC^+ production which quickly reacts with an electron forming CN. That explains why $N(CN)/N(HCN)$ ratio increases with larger radiation.

The direct photodissociation of HCN to H and CN becomes important at strong UV fields (Figure 9). *In consequence, a balance between CN and HCN depends on the UV emission of particular object, and cannot be reliably predicted by our model.* HCNH⁺ is the main parent molecule of HCN, however the photodissociation rate of HCNH⁺ is unknown. We estimated the reaction coefficient as 10% of the HCN photodissociation rate. The rough estimation is based on the electronic transition intensities predicted by quantum chemical calculations at density functional theory in extended basis set. We extended our reaction network by the HCNH⁺ photodissociation into HCN⁺ or HNC⁺, which does not affect the results. In the region of strong UV fields all molecules are subject of dissociation and ionization. This leads to the concentration of polyatomic molecules decreases, while atomic and diatomic molecules become more abundant. In consequence, new channels of CN formation are open.

Table 5: Dominant processes in CN and HCN chemistry at 50 K

| Molecule | Weak UV fields ($G_0 = 10^{-3} - 10^{-1}$) | Medium UV fields ($G_0 = 10^{-1} - 10^1$) | Strong UV fields ($G_0 = 10^1 - 10^6$) |
|----------|---|--|--|
| CN | $O + CN \rightarrow N + CO$ $CN + N \rightarrow C + N_2$ | Destruction $CN + h\nu \rightarrow C + N$ $O + CN \rightarrow N + CO$ | $CN + h\nu \rightarrow C + N$ |
| | Production $N + CH \rightarrow H + CN$ $CNC^+ + e^- \rightarrow C + CN$ $N + C_2 \rightarrow C + CN$ | Production $N + C_2 \rightarrow C + CN$ $H + CN^+ \rightarrow CN + H^+$ | $HCN^+ + e^- \rightarrow H + CN$ $N + CH \rightarrow H + CN$ $H + CN^+ \rightarrow CN + H^+$ $N + C_2 \rightarrow C + CN$ |
| HCN | $HCN + C^+ \rightarrow H + CNC^+$ $HCN^+ + HCO^+ \rightarrow CO + HCNH^+$ $HCN + H^+ \rightarrow H + HNC^+$ $HCN + h\nu \rightarrow H + CN$ | Destruction $HCN + C^+ \rightarrow H + CNC^+$ $HCN + h\nu \rightarrow H + CN$ | $HCN + h\nu \rightarrow H + CN$ $HCN + C^+ \rightarrow H + CNC^+$ |
| | Production $N + CH_2 \rightarrow H + HCN$ $H + CCN \rightarrow C + HCN$ $HCNH^+ + e^- \rightarrow H + HCN$ $C + HNC \rightarrow C + HCN$ | Production $H + CCN \rightarrow C + HCN$ $HCNH^+ + e^- \rightarrow H + HCN$ | $HCNH^+ + e^- \rightarrow H + HCN$ $H + CCN \rightarrow C + HCN$ |

5.3. Comparisons to the results from *Herschel*

Previous studies of energetic processes around low-mass protostars showed observational premises of the influence of UV radiation on molecules. These works focused on intermediate- J CO transitions (up to 6-5) that traces gas with a kinetic temperature around 100 K. With the WISH project (van Dishoeck et al. 2011) higher CO rotational transitions (up to 49-48) were studied that provided information of two temperature components seen in molecular outflows: warm with $T_{\text{rot}} \approx 300$ K and hot with $T_{\text{rot}} \approx 600 - 800$ K (Karska et al. 2013, Green et al. 2013). The observations of the water molecule shows a broad and medium-broad components associated with non-dissociative C -shocks and dissociative J -shocks respectively (Kristensen et al. 2013, Mottram et al. 2014). These spectral components can be correlated to the CO rotational temperature components (Kristensen et al. 2017). Another tracers sensitive to UV radiation, ionised hydrides such as CH^+ , OH^+ and H_2O^+ , were found in outflow cavities (Benz et al. 2016). The UV fluxes were estimated as 10^2 - 10^3 higher than average interstellar radiation. There is no molecular evidence for influence of X-rays for chemical compositions of low-mass protostars.

Most of the low-mass protostars have a broad, centred on v_{source} CO 16-15 and H_2O component in their spectra (Kristensen et al. 2017). There are typically ≈ 20 km s $^{-1}$ broad and associated with cavity shocks. The emitting gas is located in shocks along the outflow cavity wall or along the molecular wind (Yvart et al. 2016). Some of the sources show a narrow, offset component as well that is seen in the PACS CO ladder with $T_{\text{rot}} \approx 600 - 800$ K. The gas dissociated by UV photons and carried out from the protostar was proposed as an origin of the pre-shock gas (Kristensen et al. 2017). Thus, UV radiation can propagate in large scales up to 1000 AU from the central protostar, changing the properties of their surroundings. The hypothesis of the UV irradiated shocks is also raised based on H_2O/OH ratio observations. The ratio showed a few order of magnitude disagreement with fully-shielded shock models (Karska et al. 2014). The observations are reproduced with predictions of C -shock models illuminated by UV photons of the strength 0.1-10 times the interstellar value (Melnick & Kaufman 2015). The other pho-

todissociation tracers, fluxes of [OI] and [CII] are significantly higher than predicted by fully-shielded C -shock models (Karska et al. 2018). Therefore, UV radiation may play an important role in low-mass protostars surroundings.

6. Conclusions

IRAM 30 m / EMIR observations of CN and HCN emission pinpoint the location of the impact of UV radiation on the chemistry of low-mass star forming region in Serpens. A combination of simple models using radiative-code RADEX and chemical code Nahoon allows us to determine physical conditions of the gas, column densities of molecular species, and estimate the UV radiation field strength. The main conclusions of our study are the following.

- The spatial extent of HCN 1-0 and CN 1-0 show significant differences, with HCN resembling the CO 6-5 and CS 3-2 emission tracing outflows and CN concentrated close to the individual protostar positions or their groups.
- **The CN/HCN ratio is used for studying the environment of low-mass protostars for the first time.** The ratios of CN and HCN systematically differ between protostar and outflow position, both taking into account the integrated line profile and the line wings. The median of CN and HCN ratio is nearly two times lower in optically thin line wings than in the integrated line profile. The ratio is the highest at the positions of the protostars, confirming the impact of UV identified using *Herschel* as a part of the WISH program.
- For typical densities of low-mass protostellar envelopes of 10^5 cm $^{-3}$ and gas temperatures of 50 K, the chemical network for nitrogen-bearing species is sensitive to UV photons. The ratio of $N(CN)/N(HCN)$ is primarily driven by the UV radiation field, however, it should be used with care, as the relation between $N(CN)/N(HCN)$ and UV radiation field strength is not monotonic. Several reactions shape the $N(CN)/N(HCN)$ ratio. The photodissociation of HCN has an important contribution to nitrogen chemistry for $G_0 > 100$.
- The column density ratios of CN and HCN equals 1-10, ir-respectively of the gas parameters. The column density ratio

Table 6: Comparison of different line ratios

| Lines | SMM1 | SMM3r | SMM3c | SMM3b | SMM4b | Ref. |
|---|------|-------|-------|-------|-------|-----------|
| [OI] 63 μ m / o-H ₂ O 179 μ m | 8.6 | 1.3 | 2.6 | 2.2 | 2.2 | 1, 2 |
| OH 84 μ m / o-H ₂ O 179 μ m | 1.0 | 0.1 | 0.2 | 0.1 | 0.1 | 1, 2 |
| [OI] 63 μ m / OH 84 μ m | 9.0 | 9.8 | 11.4 | 13.7 | 22.2 | 1, 2 |
| H ₂ O 2 ₁₂ – 1 ₀₁ / CO 16-15 | 0.5 | 1.0 | 0.9 | 1.0 | 0.8 | 1, 2 |
| H ₂ O 4 ₀₄ – 3 ₁₃ / CO 24-23 | 0.6 | 2.0 | 0.9 | 0.5 | 0.4 | 1, 2 |
| H ₂ O 2 ₁₂ – 1 ₀₁ / H ₂ O 4 ₀₄ – 3 ₁₃ | 1.4 | 4.7 | 4.9 | 7.1 | 7.8 | 1, 2 |
| H ₂ O 2 ₂₁ – 1 ₀₁ / H ₂ O 4 ₀₄ – 3 ₁₃ | 0.2 | 3.1 | 2.3 | 3.7 | 3.0 | 1, 2 |
| CO 16-15 / CO 24-23 | 1.9 | 9.4 | 4.6 | 3.3 | 3.6 | 1, 2 |
| CN 1-0 / HCN 1-0 | 0.6 | 0.8 | 0.9 | 0.9 | 0.5 | This work |

References. (1) Goicoechea et al. (2012); (2) Dionatos et al. (2013).

cannot be reproduced by any chemical model without the UV radiation field. Our current estimations are the following: $G_0 \approx 10^1 - 10^3$ assuming 50 K and $G_0 \approx 10^2 - 10^3$ for warmer gas of 200 K. These values are in agreement with, yet in the higher end of the UV field strength obtained using H₂O and OH ratios from *Herschel*.

Similar observations for a larger sample of sources is needed to fully exploit the impact of UV radiation on the physical and chemical conditions in low-mass star forming regions. Detailed 3D modelling of protostellar envelopes with outflow cavities is necessary to fully constrain the strengths of the UV fields in physical components of young stellar objects.

Acknowledgements. AM, AK, MG and MŻ acknowledge support from the Polish National Science Center grant 2016/21/D/ST9/01098. AK acknowledges support from the First TEAM grant of the Foundation for Polish Science No. POIR.04.04.00-00-5D21/18-00 and the hospitality of the StarPlan group in the University of Copenhagen during the manuscript preparation. Support for this work was provided by the Polish National Agency for Academic Exchange through the project InterAPS. This research has made use of data from the *Herschel* Gould Belt survey (HGBS) project (<http://gouldbelt-herschel.cea.fr>). The HGBS is a *Herschel* Key Programme jointly carried out by SPIRE Specialist Astronomy Group 3 (SAG 3), scientists of several institutes in the PACS Consortium (CEA Saclay, INAF-IFSI Rome and INAF-Arcetri, KU Leuven, MPIA Heidelberg), and scientists of the *Herschel* Science Center (HSC).

References

André, P., Men'shchikov, A., Bontemps, S., et al. 2010, A&A, 518, L102
 Arce, H. G. & Sargent, A. I. 2006, ApJ, 646, 1070
 Bachiller, R., Pérez Gutiérrez, M., Kumar, M. S. N., & Tafalla, M. 2001, A&A, 372, 899
 Benz, A. O., Bruderer, S., van Dishoeck, E. F., et al. 2016, A&A, 590, A105
 Bruderer, S., Benz, A. O., Doty, S. D., van Dishoeck, E. F., & Bourke, T. L. 2009, ApJ, 700, 872
 Casali, M. M., Eiroa, C., & Duncan, W. D. 1993, A&A, 275, 195
 Cesaroni, R. 2005, Ap&SS, 295, 5
 Chapillon, E., Guilleloteau, S., Dutrey, A., Piétu, V., & Guélin, M. 2012, A&A, 537, A60
 Cravens, T. E. & Dalgarno, A. 1978, ApJ, 219, 750
 Daniel, F., Gérin, M., Roueff, E., et al. 2013, A&A, 560, A3
 Davis, C. J., Matthews, H. E., Ray, T. P., Dent, W. R. F., & Richer, J. S. 1999, MNRAS, 309, 141
 de Graauw, T., Helmich, F. P., Phillips, T. G., et al. 2010, A&A, 518, L6
 Di Francesco, J., Johnstone, D., Kirk, H., MacKenzie, T., & Ledwosinska, E. 2008, ApJS, 175, 277
 Dionatos, O., Jørgensen, J. K., Green, J. D., et al. 2013, A&A, 558, A88
 Dionatos, O., Nisini, B., Codella, C., & Giannini, T. 2010, A&A, 523, A29
 Doty, S. D. & Neufeld, D. A. 1997, ApJ, 489, 122
 Dunham, M. M., Allen, L. E., Evans, Neal J. I., et al. 2015, ApJS, 220, 11
 Enoch, M. L., Evans, Neal J. I., Sargent, A. I., & Glenn, J. 2009, ApJ, 692, 973
 Enoch, M. L., Glenn, J., Evans, Neal J. I., et al. 2007, ApJ, 666, 982
 Evans, Neal J. I., Dunham, M. M., Jørgensen, J. K., et al. 2009, ApJS, 181, 321

Frank, A., Ray, T. P., Cabrit, S., et al. 2014, Protostars and Planets VI, University of Arizona Press (2014), eds. H. Beuther, R. Klessen, C. Dullemond, Th. Henning [arXiv:1402.3553]
 Fuente, A., Martín-Pintado, J., Cernicharo, J., & Bachiller, R. 1993, A&A, 276, 473
 Fuente, A., Martín-Pintado, J., & Gaume, R. 1995, ApJ, 442, L33
 Gerin, M., Neufeld, D. A., & Goicoechea, J. R. 2016, ARA&A, 54, 181
 Goicoechea, J. R., Cernicharo, J., Karska, A., et al. 2012, A&A, 548, A77
 Goldsmith, P. F., Snell, R. L., Hemeon-Heyer, M., & Langer, W. D. 1984, ApJ, 286, 599
 Graves, S. F., Richer, J. S., Buckle, J. V., et al. 2010, MNRAS, 409, 1412
 Green, J. D., Evans, II, N. J., Jørgensen, J. K., et al. 2013, ApJ, 770, 123
 Green, J. D., Yang, Y.-L., Evans, Neal J. I., et al. 2016, AJ, 151, 75
 Griffin, M. J., Abergel, A., Abreu, A., et al. 2010, A&A, 518, L3
 Harsono, D., van Dishoeck, E. F., Bruderer, S., Li, Z. Y., & Jørgensen, J. K. 2015, A&A, 577, A22
 Harvey, P., Merín, B., Huard, T. L., et al. 2007, ApJ, 663, 1149
 Heays, A. N., Bosman, A. D., & van Dishoeck, E. F. 2017, A&A, 602, A105
 Herczeg, G. J., Karska, A., Bruderer, S., et al. 2012, A&A, 540, A84
 Hurt, R. L. & Barsony, M. 1996, ApJ, 460, L45
 Karska, A., Herczeg, G. J., van Dishoeck, E. F., et al. 2013, A&A, 552, A141
 Karska, A., Kaufman, M. J., Kristensen, L. E., et al. 2018, ApJS, 235, 30
 Karska, A., Kristensen, L. E., van Dishoeck, E. F., et al. 2014, A&A, 572, A9
 Kirk, J. M., Ward-Thompson, D., Palmeirim, P., et al. 2013, MNRAS, 432, 1424
 Klein, B., Philipp, S. D., Krämer, I., et al. 2006, A&A, 454, L29
 Könyves, V., André, P., Men'shchikov, A., et al. 2015, A&A, 584, A91
 Kristensen, L. E., van Dishoeck, E. F., Benz, A. O., et al. 2013, A&A, 557, A23
 Kristensen, L. E., van Dishoeck, E. F., Mottram, J. C., et al. 2017, A&A, 605, A93
 Lee, K. I., Fernández-López, M., Storm, S., et al. 2014, ApJ, 797, 76
 Loughnane, R. M., Redman, M. P., Thompson, M. A., et al. 2012, MNRAS, 420, 1367
 Melnick, G. J. & Kaufman, M. J. 2015, ApJ, 806, 227
 Mottram, J. C., Kristensen, L. E., van Dishoeck, E. F., et al. 2014, A&A, 572, A21
 Myers, P. C. & Ladd, E. F. 1993, ApJ, 413, L47
 Neufeld, D. A. & Dalgarno, A. 1989, ApJ, 344, 251
 Ortiz-León, G. N., Dzib, S. A., Kounkel, M. A., et al. 2017, ApJ, 834, 143
 Ossenkopf, V., Müller, H. S. P., Lis, D. C., et al. 2010, A&A, 518, L111
 Pickett, H. M., Poynter, R. L., Cohen, E. A., et al. 1998, J. Quant. Spectr. Rad. Transf., 60, 883
 Poglitsch, A., Waelkens, C., Geis, N., et al. 2010, A&A, 518, L2
 Pratap, P., Dickens, J. E., Snell, R. L., et al. 1997, ApJ, 486, 862
 Riaz, B., Thi, W. F., & Caselli, P. 2018, MNRAS, 481, 4662
 Schöier, F. L., van der Tak, F. F. S., van Dishoeck, E. F., & Black, J. H. 2005, A&A, 432, 369
 Skatrud, D. D., De Lucia, F. C., Blake, G. A., & Sastry, K. V. L. N. 1983, Journal of Molecular Spectroscopy, 99, 35
 Skrutskie, M. F., Cutri, R. M., Stiening, R., et al. 2006, AJ, 131, 1163
 Spaans, M., Hogerheijde, M. R., Mundy, L. G., & van Dishoeck, E. F. 1995, ApJ, 455, L167
 Stäuber, P., Benz, A. O., Jørgensen, J. K., et al. 2007, A&A, 466, 977
 Stäuber, P., Doty, S. D., van Dishoeck, E. F., & Benz, A. O. 2005, A&A, 440, 949
 Suresh, A., Dunham, M. M., Arce, H. G., et al. 2016, AJ, 152, 36
 Tercero, B., Cernicharo, J., Pardo, J. R., & Goicoechea, J. R. 2010, A&A, 517, A96
 Testi, L. & Sargent, A. I. 1998, ApJ, 508, L91
 van der Tak, F. F. S., Black, J. H., Schöier, F. L., Jansen, D. J., & van Dishoeck, E. F. 2007, A&A, 468, 627

- van Dishoeck, E. F. 1987, in IAU Symposium, Vol. 120, Astrochemistry, ed. M. S. Vardya & S. P. Tarafdar, 51–65
- van Dishoeck, E. F., Kristensen, L. E., Benz, A. O., et al. 2011, *PASP*, 123, 138
- van Kempen, T. A., van Dishoeck, E. F., Güsten, R., et al. 2009a, *A&A*, 507, 1425
- van Kempen, T. A., van Dishoeck, E. F., Güsten, R., et al. 2009b, *A&A*, 501, 633
- Wakelam, V., Loison, J. C., Herbst, E., et al. 2015, *ApJS*, 217, 20
- Walker-Smith, S. L., Richer, J. S., Buckle, J. V., Hatchell, J., & Drabek-Maunder, E. 2014, *MNRAS*, 440, 3568
- Wampfler, S. F., Bruderer, S., Karska, A., et al. 2013, *A&A*, 552, A56
- Wright, E. L., Eisenhardt, P. R. M., Mainzer, A. K., et al. 2010, *AJ*, 140, 1868
- Wyrowski, F., Menten, K. M., Güsten, R., & Belloche, A. 2010, *A&A*, 518, A26
- Yang, Y.-L., Green, J. D., Evans, Neal J., I., et al. 2018, *ApJ*, 860, 174
- Yıldız, U. A., Kristensen, L. E., van Dishoeck, E. F., et al. 2012, *A&A*, 542, A86
- Yıldız, U. A., Kristensen, L. E., van Dishoeck, E. F., et al. 2015, *A&A*, 576, A109
- Yıldız, U. A., Kristensen, L. E., van Dishoeck, E. F., et al. 2013, *A&A*, 556, A89
- Yvart, W., Cabrit, S., Pineau des Forêts, G., & Ferreira, J. 2016, *A&A*, 585, A74
- Zinnecker, H. & Yorke, H. W. 2007, *ARA&A*, 45, 481

Appendix A: Spectral Energy Distributions

Broad-band observations are needed in order to determine physical properties of a protostar. Dunham et al. (2015) studied protostars in the Serpens molecular cloud using 2MASS (Skrutskie et al. 2006) and Spitzer IRAC/MIPS (Evans et al. 2009), observations covering the range 1.25–70 μm , photometry from Wide-field Infrared Survey Explorer 12 and 22 μm (WISE; Wright et al. 2010), SHARC-II 350 μm (Suresh et al. 2016), the SCUBA Legacy Catalog 450 and 850 μm (Di Francesco et al. 2008) and 1.1 mm observations from Bolocam dust survey (Enoch et al. 2007). The Serpens Main region was also observed in the *Herschel* Gould Belt survey project (André et al. 2010) at 70, 160, 250, 350 and 500 μm . SPIRE/PACS photometry in the Serpens molecular cloud is discussed in Fiorellino et al. (in prep.). The flux densities used in the SED analysis are presented in Table A.1.

Based on SEDs, the bolometric temperature and luminosity can be calculated for each of the observed protostars. The bolometric luminosity is determined by integrating the SEDs over frequency:

$$L_{bol} = 4\pi d^2 \int F_\nu d\nu \quad (\text{A.1})$$

where d is the cloud distance of 436 ± 9.2 pc (Ortiz-León et al. 2017). The bolometric temperature is calculating as described in Myers & Ladd (1993):

$$T_{bol} = 1.25 \cdot 10^{-11} \bar{\nu} \quad (\text{A.2})$$

where $\bar{\nu}$ is the mean frequency given by:

$$\bar{\nu} = \frac{\int \nu F_\nu d\nu}{\int F_\nu d\nu} \quad (\text{A.3})$$

Using Scipy *splrep* and *splev* functions cubic smooth spline interpolation of the photometric data is obtained while calculating the protostars parameters. Integration along the resulting axis is obtain with the composite trapezoidal rule (*Scipy* package). The photometric data allows us to perform the integration along wide range of wavelength with exception of SMM8. Here we have only 4 photometric points from the *Herschel* Gould Belt so the calculated bolometric luminosity and temperature can be underestimated.

Appendix B: Maps in additional tracers

IRAM 30m spectral line maps in HCN and CS isotopologues are presented in Figure B.1 and Figure B.2. The H^{13}CN 1-0 emission is a sum of all hyperfine splitting components. The H^{13}CN 1-0 is spatially consistent with HCN 1-0, although a few times weaker. It peaks around Ser SMM2, Ser SMM4 and Ser SMM9, as well as at the outflow position no. 3. Except for the Ser SMM2 protostar, the peaks in H^{13}CN 1-0 are co-spatial with the HCN emission peaks. The emission of H^{13}CN 1-0 line is similarly strong in the south-east and north-west regions of the map.

The C^{34}S 3-2 line does not show such extended emission, although it is detected in all outflow positions. The emission is concentrated mostly near Ser SMM1, Ser SMM4 and Ser SMM9 sources, unlike the CS 3-2 which is not that significant around Ser SMM1. The isotopologues trace the same gas as their regular counterparts.

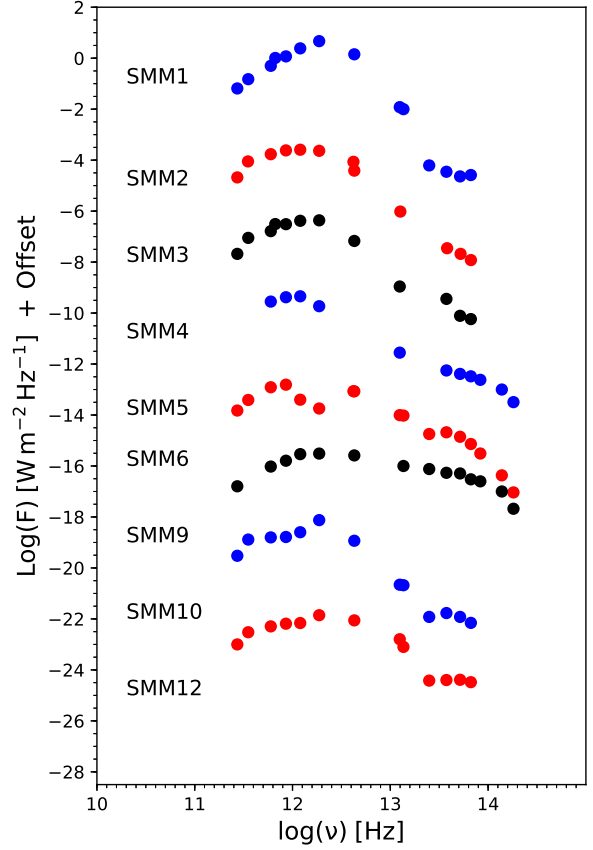


Fig. A.1: Spectral Energy Distributions of protostars in the Serpens Main region.

Appendix C: Molecular line profiles

The targeted lines are detected in most of the protostars and outflow positions. Figure C.1 shows the spectra in C^{34}S 3-2, CS 3-2, H^{13}CN 2-1, H^{13}CN 1-0, HCN 1-0 and CN 1-0 lines obtained with the IRAM 30m, as well as profiles in CO 6-5 observed with APEX-CHAMP⁺. The spectra at the Ser SMM4 position are shown in Figure 3. The H^{13}CN 2-1 line is detected only at Ser SMM4 and Ser SMM9 sources. The Ser SMM8 protostar is outside of the mapping area in CO 6-5.

Appendix D: Line fluxes and observed column densities

Table D.1 lists the observed lines and their properties calculated at protostars positions. The integrated intensity is measured at 3σ level for each spectrum separately. The peak temperature T_{peak} is the value at the maximum of a line or of the strongest hyperfine component. Column densities at the upper level N_{up} and total column densities N_{tot} are calculated as described in Section 4.1 (Equation 3 and Equation 4).

Appendix E: RADEX models

RADEX models predictions for hydrogen densities ranges from 10^4 to 10^6 cm^{-3} and kinetic temperature of a gas of 30 – 200 K are presented in Figure E.1. CN and HCN column densities ratios inferred by the models comparison with observations (blue and green rectangles) are shown in Table 4.

Table A.1: Flux densities in Jy

| λ (μm) | SMM1 | SMM2 | SMM3 | SMM4 | SMM5 | SMM6 | SMM9 | SMM10 | SMM12 |
|--------------------------------|----------------------|----------------------|----------------------|----------------------|----------------------|----------------------|----------------------|----------------------|----------------------|
| 1.25 | - | - | - | 6.0×10^{-4} | 3.0×10^{-4} | 2.1×10^{-2} | - | - | - |
| 1.65 | - | - | - | 3.2×10^{-3} | 9.0×10^{-4} | 2.1×10^{-1} | - | - | - |
| 2.17 | - | - | - | 1.0×10^{-2} | 4.3×10^{-3} | 1.0×10^0 | - | - | - |
| 3.6 | 9.0×10^{-4} | 4.0×10^{-4} | 2.8×10^{-3} | 2.4×10^{-2} | 3.1×10^{-2} | 2.5×10^0 | 2.0×10^{-3} | 7.4×10^{-3} | 2.8×10^{-3} |
| 4.5 | 2.6×10^{-3} | 1.2×10^{-3} | 5.8×10^{-3} | 3.3×10^{-2} | 7.3×10^{-2} | 3.0×10^0 | 7.0×10^{-3} | 3.3×10^{-2} | 3.0×10^{-2} |
| 5.8 | 2.3×10^{-3} | 2.1×10^{-3} | 7.8×10^{-3} | 4.1×10^{-2} | 1.4×10^{-1} | 5.1×10^0 | 1.2×10^{-2} | 4.1×10^{-2} | 1.0×10^{-1} |
| 8.0 | 3.5×10^{-3} | 3.5×10^{-3} | 3.6×10^{-2} | 5.6×10^{-2} | 2.1×10^{-1} | 5.4×10^0 | 1.7×10^{-2} | - | 2.0×10^{-1} |
| 12.0 | 6.2×10^{-3} | - | - | - | 1.8×10^{-1} | 7.6×10^0 | 1.2×10^{-2} | 3.8×10^{-2} | 2.2×10^{-1} |
| 22.0 | 1.0×10^0 | - | - | - | 9.5×10^{-1} | 1.0×10^1 | 2.1×10^{-1} | 8.0×10^{-1} | 3.1×10^0 |
| 24.0 | 1.2×10^0 | 1.0×10^{-1} | 1.1×10^{-1} | 2.8×10^{-1} | 9.9×10^{-1} | - | 2.2×10^{-1} | 1.6×10^0 | 2.6×10^0 |
| 70.0 | 1.4×10^2 | 3.9×10^0 | 6.8×10^0 | - | 8.5×10^0 | 2.6×10^1 | 1.2×10^1 | 8.8×10^0 | 3.3×10^0 |
| 160.0 | 4.7×10^2 | 2.3×10^1 | 4.4×10^1 | 1.9×10^1 | 1.8×10^0 | 3.1×10^1 | 7.5×10^1 | 1.4×10^1 | 2.0×10^1 |
| 250.0 | 2.4×10^2 | 2.6×10^1 | 4.2×10^1 | 4.6×10^1 | 4.0×10^0 | 2.9×10^1 | 2.5×10^1 | 6.9×10^0 | 3.2×10^1 |
| 350 | 1.2×10^2 | 2.4×10^1 | 3.1×10^1 | 4.2×10^1 | 1.6×10^1 | 1.6×10^1 | 1.6×10^1 | 6.5×10^0 | 3.1×10^1 |
| 450.0 | 1.0×10^2 | - | 3.1×10^1 | - | - | - | - | - | - |
| 500 | 5.0×10^1 | 1.7×10^1 | 1.6×10^1 | 2.8×10^1 | 1.2×10^1 | 9.5×10^0 | 1.6×10^1 | 5.1×10^0 | 1.6×10^1 |
| 850.0 | 1.5×10^1 | 8.9×10^0 | 8.9×10^0 | - | 3.9×10^0 | - | 1.3×10^1 | 3.0×10^0 | - |
| 1100.0 | 6.5×10^0 | 2.1×10^0 | 2.1×10^0 | - | 1.5×10^0 | 1.6×10^0 | 3.0×10^0 | 1.0×10^0 | 2.1×10^0 |

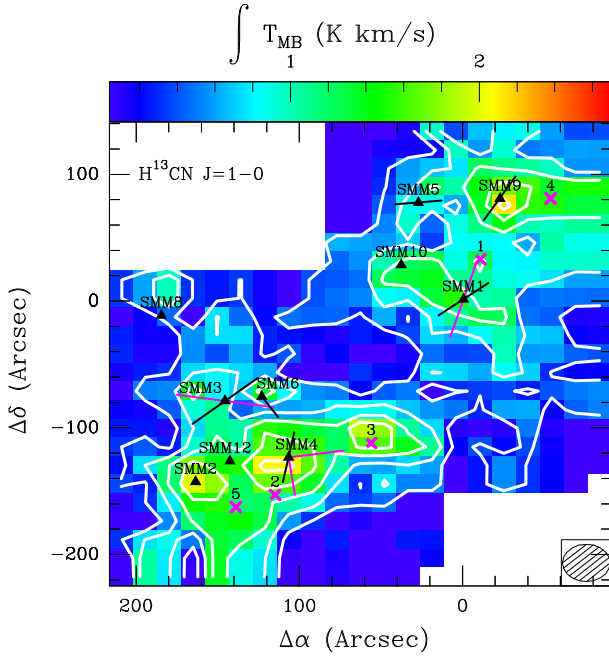


Fig. B.1: Similar to Figure 2 but for $\text{H}^{13}\text{CN } J = 1 - 0$ line. The first contour is at 10σ level, with step of 10σ .

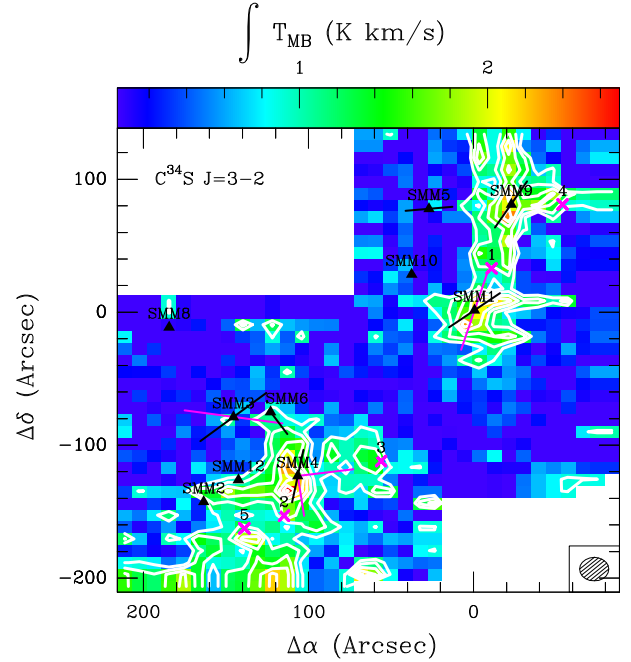


Fig. B.2: Similar to Figure 2 but for $\text{C}^{34}\text{S } J = 3 - 2$ line. The first contour is at 30σ level, with step of 10σ .

Appendix F: Dominant reactions in CN, HCN chemistry

Dominant processes in CN and HCN reactions modelled at a temperature of 50 K are listed in Table 5. The processes are illustrated in the Nahoon model parameter space: main channels of HCN and CN destruction, as well as HCN and CN production (Figure 10 and Figure F.1 - Figure F.3 respectively). Only the reactions contributing at least 30% in total flux are taken into consideration. Dominant reactions are more dependent on the strength of the UV radiation than on the hydrogen density. Reaction networks for UV radiation in weak ($G_0 = 10^{-4} - 10^{-1}$),

intermediate ($G_0 = 10^{-1} - 10^1$) and strong ($G_0 = 10^1 - 10^6$) regime are presented in Figure F.4, Figure F.5 and Figure 9 respectively. Not only the dominant reactions, but also the main route of the reactants production are illustrated. The dominant processes modelled assuming the temperature of 200 K are listed in Table F.1.

Appendix G: Correlations with T_{bol} and L_{bol}

Figure G.1 compares the luminosity in CN 1-0, HCN 1-0 and CS 3-2 lines in respect to the bolometric luminosities and temperatures of the observed protostars. A molecule luminosity is

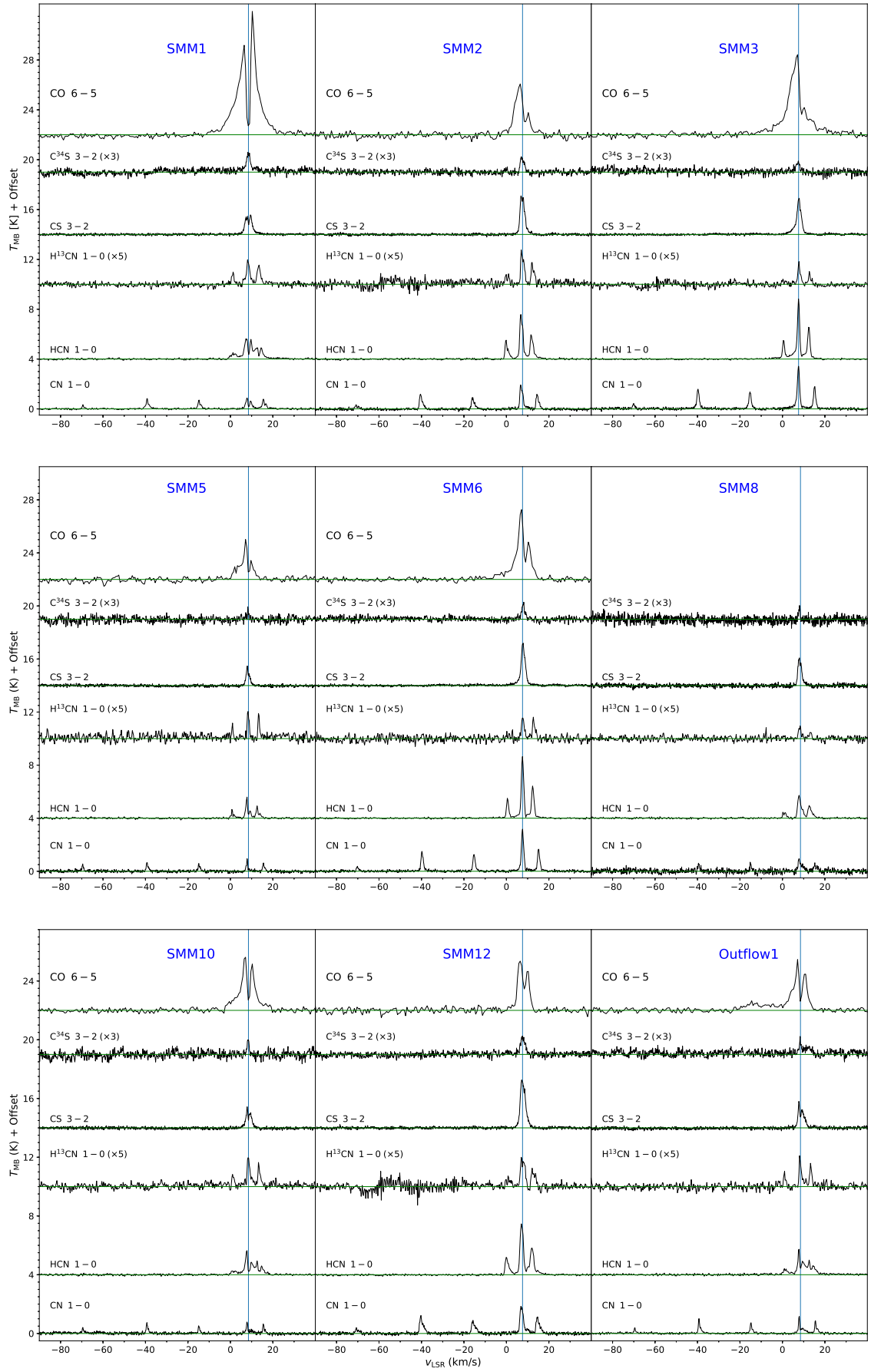


Table D.1: Integrated fluxes of the observed line at the positions of protostars

| Line | | SMM1 | SMM2 | SMM3 | SMM4 | SMM5 | SMM6 | SMM8 | SMM9 | SMM10 | SMM12 |
|------------------------|---|----------------------|----------------------|----------------------|----------------------|----------------------|----------------------|----------------------|----------------------|----------------------|----------------------|
| CN 1-0 | $\int T_{\text{mb}} dV$ (K km s ⁻¹) | 6.29 | 8.52 | 12.16 | 10.22 | 2.72 | 10.62 | 2.97 | 4.90 | 2.96 | 10.06 |
| | T_{peak} (K) | 0.89 | 1.92 | 3.42 | 1.90 | 0.94 | 3.17 | 0.94 | 0.84 | 0.78 | 1.85 |
| | N_{up} (cm ⁻²) | 1.3×10 ¹³ | 1.8×10 ¹³ | 2.6×10 ¹³ | 2.2×10 ¹³ | 5.7×10 ¹² | 2.2×10 ¹³ | 6.2×10 ¹² | 1.0×10 ¹³ | 6.2×10 ¹² | 2.1×10 ¹³ |
| | N_{tot} (cm ⁻²) | 7.9×10 ¹⁴ | 1.1×10 ¹⁵ | 1.5×10 ¹⁵ | 1.3×10 ¹⁵ | 3.4×10 ¹⁴ | 1.3×10 ¹⁵ | 3.7×10 ¹⁴ | 6.2×10 ¹⁴ | 3.7×10 ¹⁴ | 1.3×10 ¹⁵ |
| HCN 1-0 | $\int T_{\text{mb}} dV$ (K km s ⁻¹) | 10.34 | 13.08 | 14.36 | 21.67 | 4.04 | 13.10 | 6.84 | 20.68 | 7.26 | 14.24 |
| | T_{peak} (K) | 1.76 | 3.48 | 4.95 | 4.69 | 1.72 | 5.15 | 1.72 | 2.40 | 1.75 | 3.50 |
| | N_{up} (cm ⁻²) | 6.5×10 ¹² | 8.3×10 ¹² | 9.1×10 ¹² | 1.4×10 ¹³ | 2.6×10 ¹² | 8.3×10 ¹² | 4.3×10 ¹² | 1.3×10 ¹³ | 4.6×10 ¹² | 9.0×10 ¹² |
| | N_{tot} (cm ⁻²) | 2.5×10 ¹⁴ | 3.1×10 ¹⁴ | 3.4×10 ¹⁴ | 5.2×10 ¹⁴ | 9.6×10 ¹³ | 3.1×10 ¹⁴ | 1.6×10 ¹⁴ | 4.9×10 ¹⁴ | 1.7×10 ¹⁴ | 3.4×10 ¹⁴ |
| CS 3-2 | $\int T_{\text{mb}} dV$ (K km s ⁻¹) | 5.89 | 8.56 | 8.30 | 14.76 | 2.56 | 8.50 | 4.51 | 12.43 | 3.58 | 9.88 |
| | T_{peak} (K) | 1.57 | 3.10 | 2.90 | 4.30 | 1.48 | 3.2 | 2.08 | 2.70 | 1.43 | 3.26 |
| | N_{up} (cm ⁻²) | 4.1×10 ¹² | 5.9×10 ¹² | 5.7×10 ¹² | 1.0×10 ¹³ | 1.8×10 ¹² | 5.7×10 ¹² | 3.1×10 ¹² | 8.6×10 ¹² | 2.5×10 ¹² | 6.8×10 ¹² |
| | N_{tot} (cm ⁻²) | 4.5×10 ¹³ | 6.5×10 ¹³ | 6.3×10 ¹³ | 1.1×10 ¹⁴ | 2.0×10 ¹³ | 6.5×10 ¹³ | 3.4×10 ¹³ | 9.5×10 ¹³ | 2.7×10 ¹³ | 7.5×10 ¹³ |
| C ³⁴ S 3-2 | $\int T_{\text{mb}} dV$ (K km s ⁻¹) | 1.27 | 0.86 | 0.50 | 1.49 | 0.32 | 0.76 | 0.26 | 1.83 | 0.39 | 0.56 |
| | T_{peak} (K) | 0.56 | 0.47 | 0.36 | 0.64 | 0.42 | 0.56 | 0.35 | 0.62 | 0.40 | 0.42 |
| | N_{up} (cm ⁻²) | 7.1×10 ¹¹ | 4.8×10 ¹¹ | 2.8×10 ¹¹ | 8.4×10 ¹¹ | 1.8×10 ¹¹ | 4.3×10 ¹¹ | 1.4×10 ¹¹ | 1.0×10 ¹² | 2.2×10 ¹¹ | 3.1×10 ¹¹ |
| | N_{tot} (cm ⁻²) | 7.9×10 ¹² | 5.4×10 ¹² | 3.1×10 ¹² | 9.4×10 ¹² | 2.0×10 ¹² | 4.8×10 ¹² | 1.6×10 ¹² | 1.2×10 ¹³ | 2.5×10 ¹² | 3.5×10 ¹² |
| H ¹³ CN 1-0 | $\int T_{\text{mb}} dV$ (K km s ⁻¹) | 1.59 | 1.50 | 0.55 | 1.61 | 0.77 | 0.87 | 0.14 | 2.37 | 1.04 | 1.61 |
| | T_{peak} (K) | 0.45 | 0.64 | 0.41 | 0.61 | 0.42 | 0.40 | 0.21 | 0.38 | 0.45 | 0.46 |
| | N_{up} (cm ⁻²) | 3.3×10 ¹¹ | 3.1×10 ¹¹ | 1.6×10 ¹¹ | 3.4×10 ¹¹ | 1.6×10 ¹¹ | 1.8×10 ¹¹ | 2.9×10 ¹⁰ | 5.0×10 ¹¹ | 2.2×10 ¹¹ | 3.4×10 ¹¹ |
| | N_{tot} (cm ⁻²) | 1.3×10 ¹³ | 1.2×10 ¹³ | 4.5×10 ¹² | 1.3×10 ¹³ | 6.2×10 ¹² | 7.0×10 ¹² | 1.1×10 ¹² | 1.9×10 ¹³ | 8.4×10 ¹² | 1.3×10 ¹³ |

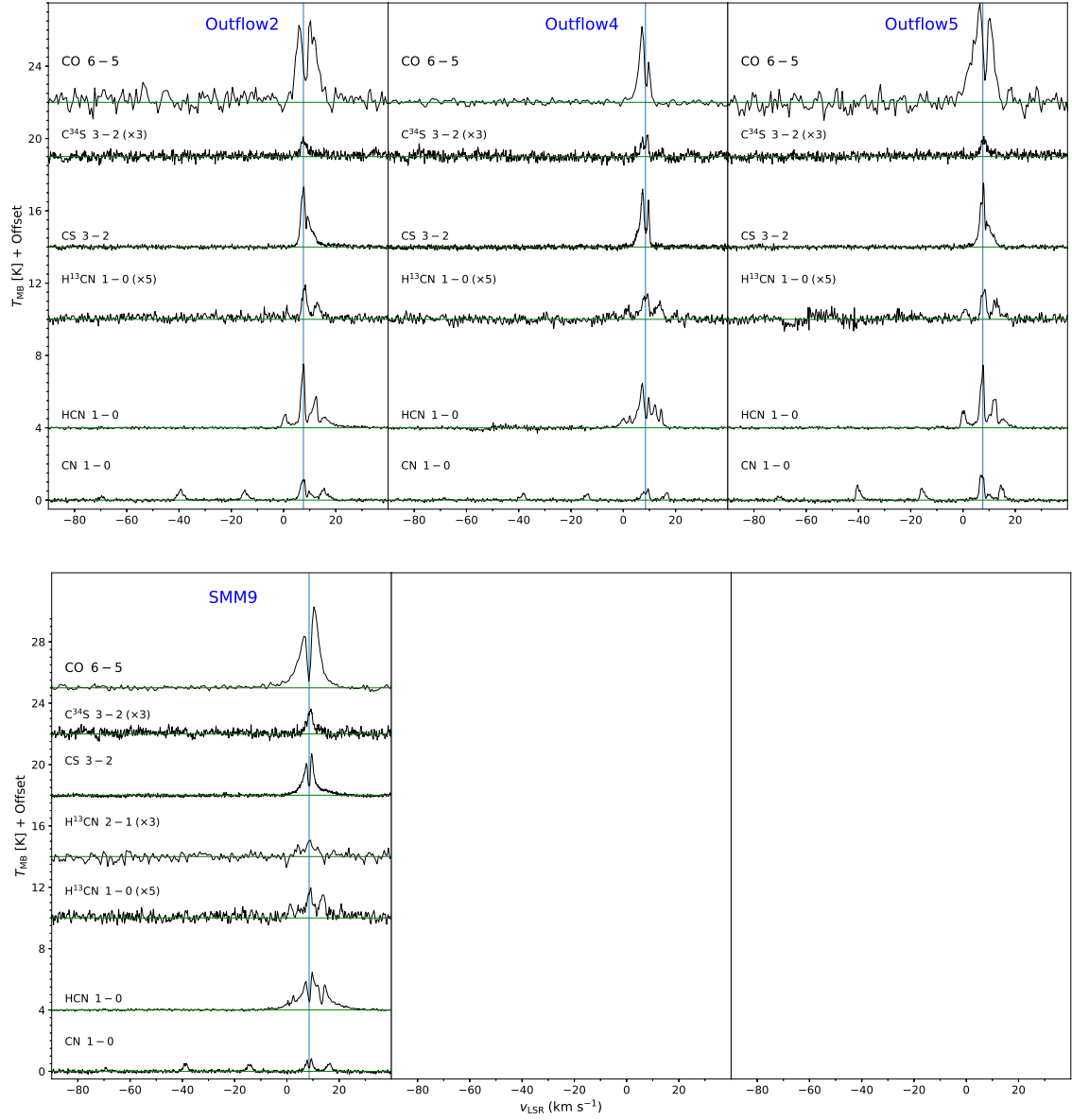


Fig. C.1: Serpens Main sources spectra of CO 6-5, $C^{34}S$ 3-2, CS 3-2, $H^{13}CN$ 2-1, $H^{13}CN$ 1-0, HCN 1-0 and CN 1-0 lines.

calculated based on the integrated intensity of a line at 3σ level. The integrated flux in $K km s^{-1}$ unit is converted to $Jy km s^{-1}$ using conversion factors Jy/K tabularised in 'Proposals for IRAM Telescopes' document³. The luminosity in a line is calculated by the standard relation between luminosity L and flux F (Equation G.1) and expressed in solar luminosities, where distance d is 436 ± 9.2 pc (Ortiz-León et al. 2017).

$$L = F 4 \pi d^2 \quad (G.1)$$

³ <https://www.iram.fr/GENERAL/calls/w07/w07/node33.html>

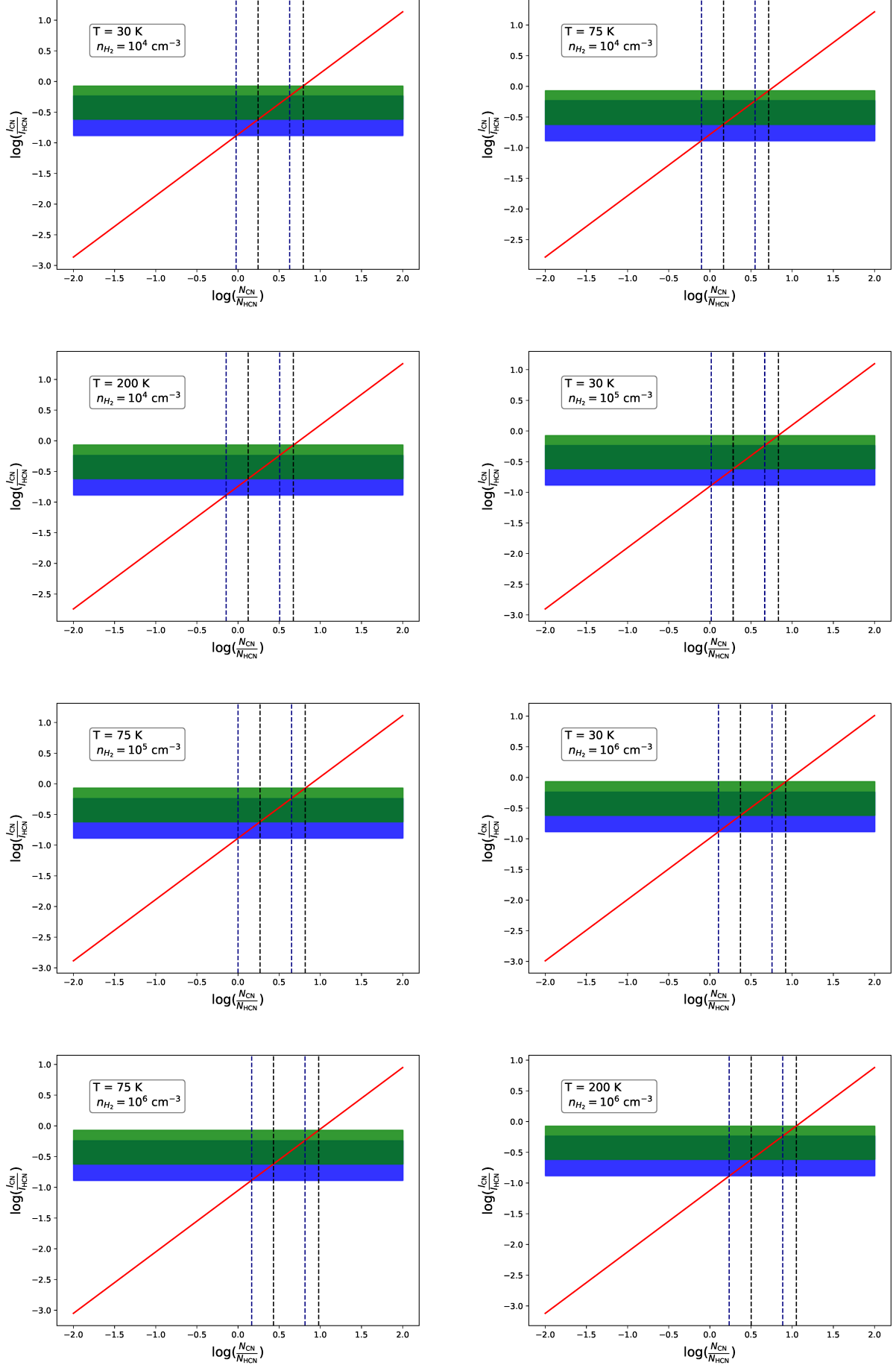


Fig. E.1: RADEX models for different parameters. Similar to Figure 4. Article number, page 19 of 22

Table F.1: Dominant processes in CN, HCN chemistry - outflow (200K)

| Molecule | Weak UV fields ($G_0 = 10^{-4} - 10^{-1}$) | Medium UV fields ($G_0 = 10^{-1} - 10^1$) | Strong UV fields ($G_0 = 10^1 - 10^6$) |
|----------|--|--|---|
| CN | | Destruction | |
| | $O + CN \rightarrow N + CO$ $CN + N \rightarrow C + N_2$ | $CN + h\nu \rightarrow C + N$ $O + CN \rightarrow N + CO$ | $CN + h\nu \rightarrow C + N$ |
| | | Production | |
| | $CNC^+ + e^- \rightarrow C + CN$ $N + C_2 \rightarrow C + CN$ $HCN + h\nu \rightarrow H + CN$ | $N + C_2 \rightarrow C + CN$ $H + CN^+ \rightarrow CN + H^+$ | $H + CN^+ \rightarrow CN + H^+$ $HCN^+ + e^- \rightarrow H + CN$ $N + C_2 \rightarrow C + CN$ $N + CH \rightarrow H + CN$ $HCN + h\nu \rightarrow H + CN$ |
| HCN | | Destruction | |
| | $HCN + C^+ \rightarrow H + CNC^+$ $HCN + h\nu \rightarrow H + CN$ $HCN + HCO^+ \rightarrow CO + HCNH^+$ | $HCN + C^+ \rightarrow H + CNC^+$ $HCN + h\nu \rightarrow H + CN$ | $HCN + h\nu \rightarrow H + CN$ $HCN + C^+ \rightarrow H + CNC^+$ |
| | | Production | |
| | $N + CH_2 \rightarrow H + HCN$ $H + CCN \rightarrow C + HCN$ $CN + H_2 \rightarrow H + HCN$ $C + HNC \rightarrow C + HCN$ | $H + CCN \rightarrow C + HCN$ $HCNH^+ + e^- \rightarrow H + HCN$ | $HCNH^+ + e^- \rightarrow H + HCN$ $H + CCN \rightarrow C + HCN$ $H_2NC^+ + e^- \rightarrow H + HCN$ $N + CH_2 \rightarrow H + HCN$ |

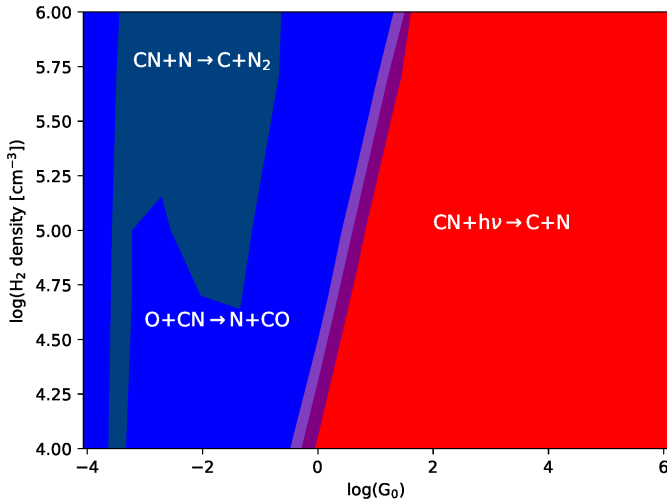


Fig. F.1: Dominant reactions of CN destruction. Reactions contributed at least 50% of total flux are marked with full colours. Transparent colours correspond to 30%-50% contribution. $CN + h\nu \rightarrow C + N$ reaction is marked with red colour, $O + CN \rightarrow N + CO$ with blue colour and $CN + N \rightarrow C + N_2$ with green colour.

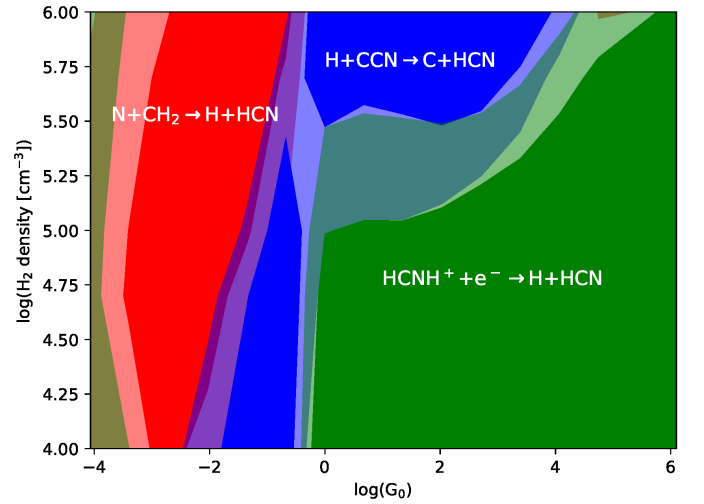


Fig. F.2: Similar to Figure F.1 but for HCN production. $HCNH^+ + e^- \rightarrow H + HCN$ reaction is marked with green colour, $H + CCN \rightarrow C + HCN$ with blue colour and $N + CH_2 \rightarrow H + HCN$ with red colour.

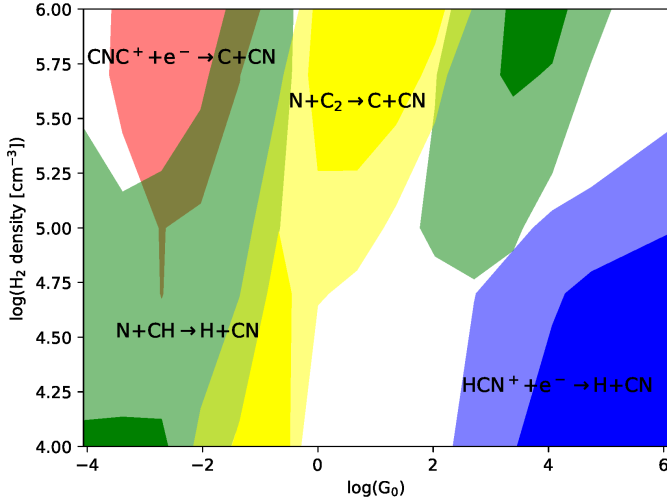


Fig. F.3: Similar to Figure F.1 but for CN production. **$\text{HCN}^+ + \text{e}^- \rightarrow \text{H} + \text{CN}$ reaction is marked with blue colour, $\text{N} + \text{C}_2 \rightarrow \text{C} + \text{CN}$ with yellow colour, $\text{CNC}^+ + \text{e}^- \rightarrow \text{C} + \text{CN}$ with red colour and $\text{N} + \text{CH} \rightarrow \text{H} + \text{CN}$ with green colour.**

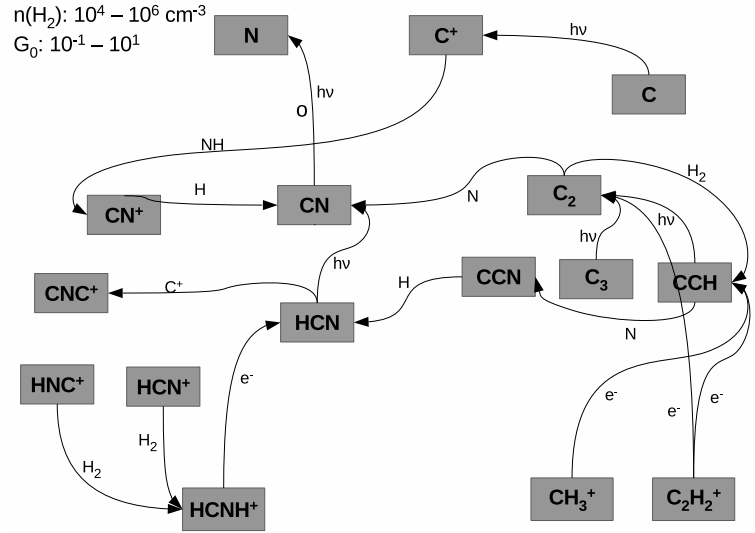


Fig. F.5: Similar to Figure F.4 but for UV field of $G_0 = 10^{-1} - 10^1$.

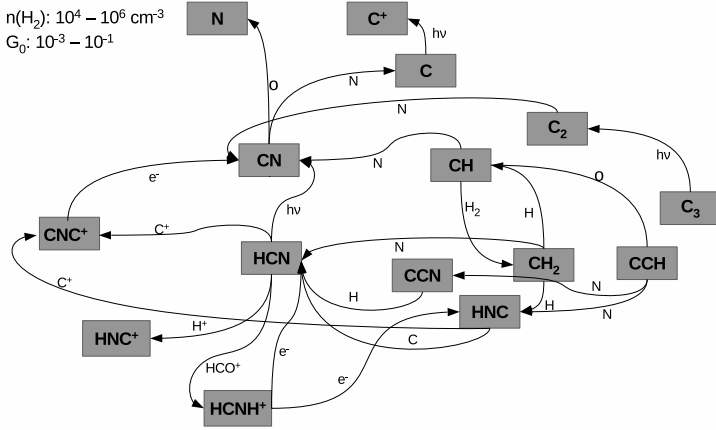


Fig. F.4: Reactions network for weakly UV irradiated gas.

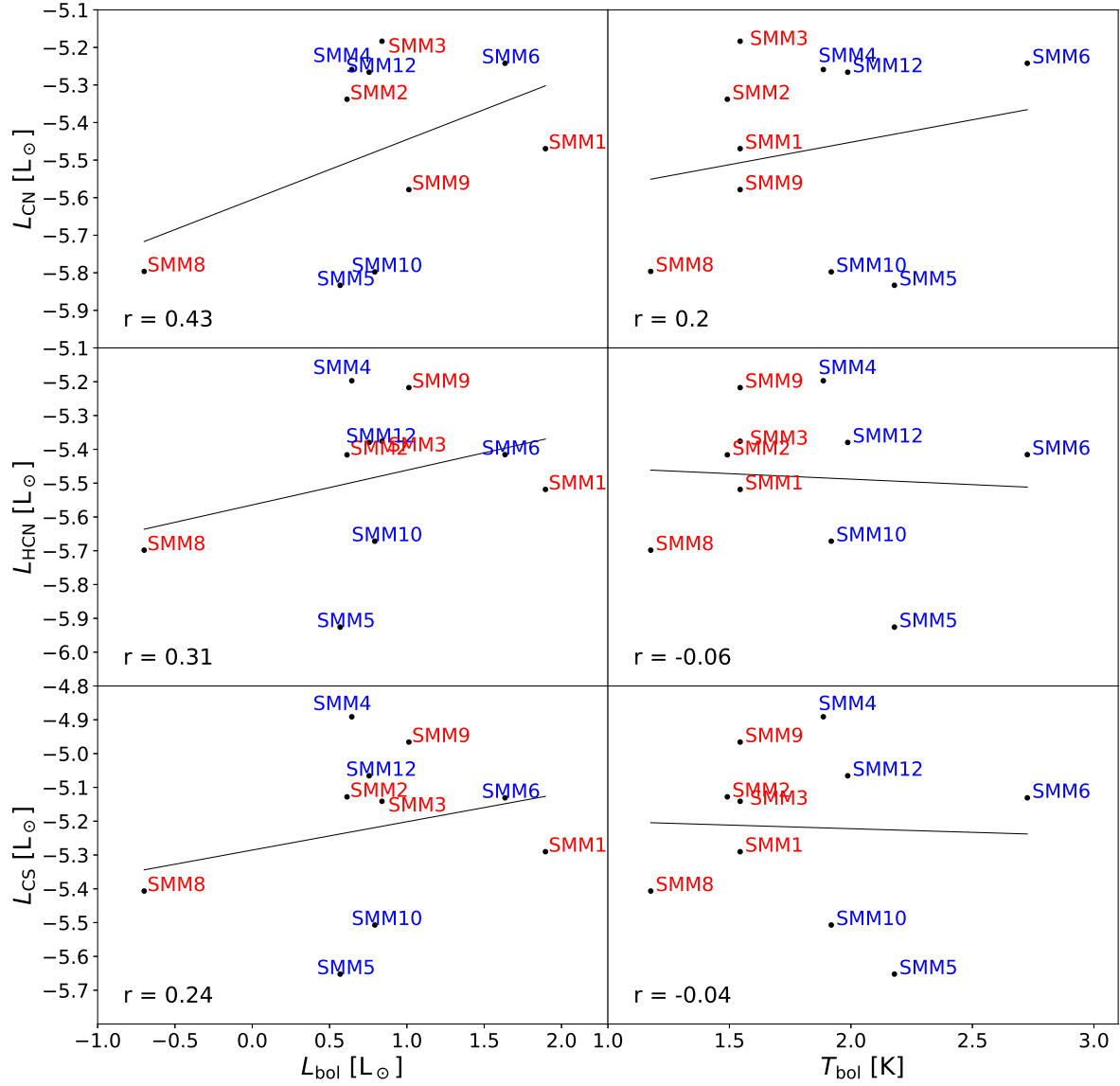


Fig. G.1: Correlations of lines luminosity with bolometric luminosity and temperature of protostars. Class 0 protostars are marked with red, while Class I with blue colour. The Pearson coefficient of the correlation (r) is shown.